Synthetic Antigen Presenting cells reveal the diversity and functional specialisation of extracellular vesicles composing the fourth signal of T cell immunological synapses.

Pablo F. Céspedes[1,11], Ashwin Jainarayanan[1,11], Lola Fernández-Messina[2,3], Salvatore Valvo[1], David G. Saliba[1], Audun Kvalvaag[1], Elke Kurz[1], Huw Colin-York[1,4], Marco Fritzsche[1,4], Yanchun Peng[4,5], Tao Dong[4,5], Jesús A. Siller-Farfán[6], Omer Dushek[6], Michal Maj[6], Erdinc Sezgin[7], Ben Peacock[8], Alice Law[8], Dimitri Aubert[8], Simon Engledow[9], Moustafa Attar[1,9], Svenja Hester[10], Roman Fischer[10], Francisco Sánchez-Madrid[2,3], Michael L. Dustin[1].

Affiliations:

1. Kennedy Institute of Rheumatology, Nuffield Department of Orthopedics, Rheumatology and Musculoskeletal Sciences, The University of Oxford, Oxford, UK.
2. Immunology Service, Hospital de la Princesa, Instituto Investigación Sanitaria Princesa, Universidad Autónoma de Madrid, Madrid, Spain.
3. Intercellular communication in the inflammatory response. Vascular Physiology Area, Centro Nacional de Investigaciones Cardiovasculares (CNIC), Madrid, Spain.
4. MRC Human Immunology Unit, MRC Weatherall Institute of Molecular Medicine, Radcliffe Department of Medicine, The University of Oxford, Oxford, UK.
5. Chinese Academy of Medical Science (CAMS) Oxford Institute (COI), University of Oxford, Oxford, UK.
6. Sir William Dunn School of Pathology, The University of Oxford, Oxford, UK.
7. Science for Life Laboratory, Department of Women's and Children's Health, Karolinska Institutet, Stockholm, Sweden.
8. NanoFCM, MediCity, Nottingham, UK.
9. Oxford Genomics Centre, Wellcome Centre for Human Genetics, The University of Oxford, Oxford, UK.
10. Target Discovery Institute, Centre for Medicines Discovery, Nuffield Department of Medicine, The University of Oxford, Oxford, UK.
11. These authors contributed equally to this work.

ABSTRACT

The T cell Immunological Synapse (IS) is a pivotal hub for the regulation of adaptive immunity by facilitating the exchange of information between cells engaged in physical contact. Beyond the integration of antigen (signal one), co-stimulation (signal two), and cytokines (signal three), the IS facilitates the delivery of T-cell effector assemblies including supramolecular attack particles (SMAPs) and extracellular vesicles (EVs). How these particulate outputs differ among T -cell subsets and how subcellular compartments and signals exchanged at the synapse contribute to their composition is not fully understood. Here we harnessed bead-supported lipid bilayers (BSLBs) as a tailorable and versatile technology to study synaptic particle biogenesis and composition in different T-cell subsets, including CART. These synthetic antigen-presenting cells (APCs) facilitated the characterisation of synaptic vesicles (SVs) as a heterogeneous population of EVs comprising among others plasma membrane-derived synaptic ectosomes and $CD63^+$ exosomes. We harnessed BSLB to unveil the factors influencing the vesicular release of CD40L, as a model effector, identifying CD40 *trans*-presentation, T-cell activation, ESCRT upregulation/recruitment, antigen density/potency, co-repression by PD-1 ligands, and its processing by ADAM10 as major determinants. Further, BSLB made possible the comparison of microRNA (miR) species associated with SVs and steadily shed EVs (sEVs). Altogether, our data provide evidence for a higher specialisation of SVs which are enriched not only in effector immune receptors but also in miR and RNA-binding proteins. Considering the molecular uniqueness and functional complexity of the SV output, which is also accompanied by SMAPs, we propose their classification as signal four.

Keywords: T cells, extracellular vesicles, regulatory T cells, cytotoxic T cells, chimeric antigen receptor-expressing T cells (CART), synaptic ectosomes, synaptic vesicles, CD40L,

miRNA, CD38, CD39, CD73, CD80, CD86, PD-L1, PD-L2, HIV gp120, ADAM10, BST2 and CD81.

INTRODUCTION

T lymphocytes are key players in the regulation and escalation of adaptive immunity. Helper T cells (TH), cytotoxic T lymphocytes (CTL) and regulatory T cells (Treg) shape cellular networks through the assembly of physical interactions termed Immunological Synapses (IS) with other cells. The concerted rearrangement of receptors and their bound ligands at the cell-cell interface increases the efficiency of signal transduction increasing the sensitivity of T cells for antigens and other interfacial signals including co-stimulatory and co-repressing signals. Similarly, the surface rearrangement of adhesion molecules at the IS provides physical stability and supports the regulated and bidirectional relay of effector particles including plasma membrane (PM)-derived extracellular vesicles (EVs) termed synaptic ectosomes (SE), and supramolecular attack particles (SMAPs) [1-3]. These synaptic particles thus mediate a variety of effects including the functional modulation of acceptor cells and their lysis [4]. Most remarkably, pathogen evolution has taken advantage of the cellular machineries mediating SE budding. For instance, HIV-1 proteins Gag and gp120 facilitate the transfer of viral information among interacting cells by hijacking components of the endosomal sorting complexes required for transport (ESCRT) system [1, 5, 6].

T-cell derived EVs have captured attention in recent years as vehicles for a number of effectors, including microclusters of immunoreceptors in the case of SE [1, 2] and enzymes, small RNAs[7, 8] and mitochondrial DNA[9] in the case of exosomes. However, 1) whether EVs secreted at the IS here globally referred to as synaptic vesicles (SV), differ to those EVs steadily shed by T cells (sEV); and 2) whether they include more than SE, has not yet been evaluated. The biological relevance of the IS as a hub for the transfer of information in a

context of specificity provided by antigens, suggests that although SV and sEV share an evolutionarily conserved budding machinery [10], their effector composition and biogenesis might differ to accommodate different modes of intercellular communication. As such, comprehensive tools capable of evaluating how different intercellular signals define the vesicular output of the IS, and how these compare to sEVs, are needed. Current microscopy methods used in the study of the IS effector output require imaging high number of cells per condition, being low throughput and non-compatible with the purification of SVs for downstream analyses. As a first approach to tackle these needs, here we present bead-supported lipid bilayers (BSLBs) as highly tailorable and scalable synthetic antigen-presenting cells (APCs) facilitating the dissection of information transfer at T cell IS. We harnessed this technology to identify the hallmarks of SV composition and the major factors influencing their release. The imaging of SV marker distribution in T cell synapses with total internal reflection microscopy (TIRFM) validated our findings and helped expanding our characterization of vesicle-associated synaptic effectors. Numerous examples of protein and microRNA (miR) transfer to BSLB correlate with the mobilisation of proteins, such as CD40L, CD39, CD63, CD73, CD81, and BST2, as well as RNA-puncta and RNA-binding proteins to the synaptic cleft. Furthermore, BSLB allowed the first side by side comparison of miR species and RNA-binding proteins (RBPs) associated to SV and sEVs. Altogether, these data collected thanks to the use of BSLB suggest that SVs represent EVs highly specialised in the delivery of intercellular messengers including immune receptors and miRs.

RESULTS

BSLBs facilitate the capture and characterisation of the T cell synaptic output.

We have previously shown that reconstituting BSLB with anti-CD3ε Fab, ICAM1 and combinations of CD40 and ICOSL instigated the transfer of SE containing TCR, CD40L

and ICOS to BSLB in a ligand-specific manner [2]. This first generation of BSLB used EDTA to release the adhesion molecule ICAM1 and promote the dissociation of cells and BSLB while retaining TCR^+ SE tethered to anti-CD3ε Fab anchored to BSLB via biotin-streptavidin. To study other vesicle populations and extend the analytical capabilities of BSLB, we developed a 14 His-tagged anti-CD3ε Fab allowing the tailoring of BSLB as synthetic APCs providing the flexibility to study T cell SV as both bulk *on bead* populations and as single *eluted* vesicles (please refer to Methods). As good APC surrogates, BSLBs displayed lipid bilayer and anti-CD3ε Fab diffusion coefficients of 3.2 ± 0.79 and 0.68 ± 0.39 $\mu m^2/s$, respectively (Fig. 1A), which are comparable to physiological ranges reported for native PM lipids and proteins [11-13].

The time lapse imaging of unperturbed co-cultures demonstrated that BSLB instigated an active transfer of CD40L from stimulated T cells, which left a "synaptic stamp" on the engaged BSLBs (Fig. 1B). We used gradual cooling down of cell: BSLB conjugates to promote their dissociation while minimizing mechanical stress of BSLB and their tethered EVs. This favoured the downstream analysis of SV with several different techniques including imaging, conventional and Nano flow cytometry (FCM). Imaging FCM, demonstrated the presence of similar vesicular stamps positive for TCR, CD81 and CD38 on single BSLB (Fig. 1C and S1A-B), showing higher spatial colocalization of TCR, with EV markers CD38 and CD81, compared to CD4, and proteins homogeneously coating BSLBs (ICAM-1 and α-CD3ε Fab at 200 molec./μm^2; Fig. S1C). T cells acquired little ICAM1 and fluorescent lipids (DOPE) from BSLB indicating a limited *trans* endocytosis of and the overall structural integrity of BSLB (Fig. S1D), even at densities in which T cells transferred a substantial fraction of their TCRαβ heterodimer (Fig 1D).

We further characterised the material composing the synaptic stamps deposited on BSLB by triggering the releasee of transferred material using ice-cold EDTA. Elution led to a

significant release of most of the TCR and CD40L content on BSLB (Fig. 1E-F). TEM images of the material further purified using differential centrifugation revealed the presence of recombinant proteins and cell-derived vesicles, the latter of which measured 123 ± 12.1 nm as determined by nanoparticle tracking analyses (NTA) (size range between 50 and 300 nm, Fig. S1C). NanoFCM analysed further revealed a bulk size average of 82.13 ± 0.75 nm and 84.4 ± 5.99 nm for SV eluted from BSLB (Table S1), which were consistent with our previous EM and dSTORM measurements [1, 2], and a bulk median size of 65 ± 25 nm (Table S1 and Fig. S2A) for sEV. We further used nanoFCM to compare size distributions of marker-specific vesicles present in SV and sEV collected from the supernatant of syngeneic T cells. Based in our initial characterization of SE markers [2], we then performed a more careful examination and comparison of TCR, CD63, CD40L and BST2 positive events between SV and sEV. NanoFCM analyses revealed an overall larger median size of SV compared to sEV (Fig. S2B), also displaying a higher expression of TCR and CD40L (Fig. 1H-K). Interestingly, the percentage of $CD63^+$ SV was negligible compared to TCR^+ vesicles (Fig. S2C, *top*), which is explained partly by the resistance of $CD63^+$ SV to EDTA elution (Fig. S2C, *bottom*). Overall, $CD63^+$, TCR^+, $BST2^+$ and $CD40L^+$ SV displayed a different size distribution (Fig. S2B), indicating a highly heterogeneous population of vesicles being released at the IS and intrinsically different in size and protein loads to sEV. TIRFM imaging of TH synapses further corroborated the high heterogeneity and spatial segregation of $CD40L^+$ and $CD63^+$, $CD81^+$, and $BST2^+$ in vesicles released in the synaptic cleft (Fig. S2D), or as part of vesicular tracks shed by cells resuming migration (Fig. S2E, F-H). Immunoblotting of eluted fractions further demonstrated the presence of the 25 kDa membrane-anchored form of CD40L in SV (Fig. S2I), suggesting minimal contribution of enzymatically shed CD40L on the overall transfer to BSLB. The larger overall size of TCR^+

and $CD40L^+$ SV might relate to the inclusion of >80 nm microclusters in budding ectosomes [2], which might represent a major subpopulation of SVs.

The differences in SV size, protein loads, and spatial distribution observed for CD40L, TCR, CD63 and BST2 suggest a highly heterogeneous population of effector SV shed in the synaptic cleft. Likely, this results from various converging organelle vesicles transporting cargo to the pole of stimulated T cells. With this in mind, we performed acute pharmacological inhibition of TH cells before and during incubation with BSLB to understand the contribution of subcellular compartments to the overall SV output. We used a panel of 12 inhibitors targeting among others cytoskeleton dynamics and the transport of vesicular cargo from different organelles including ER and Golgi-associated cisternae (Table S2 and Fig. S3). Since cell surface expression levels were differentially affected by the inhibitors tested (Fig. S3A), we used a normalised SV transfer metric based on the maximum level of TCR^+, $CD40L^+$, $BST2^+$ and $CD63^+$ SV transferred to BSLB measured in untreated controls ($\%T_{max}$).

Except for actin cytoskeleton disruptors Latrunculin A and Jasplakinolide, most inhibitors did not affect synapse stability significantly as evidenced by the percent of remaining cell: BSLB conjugates following cold incubation (Fig. S3B). With comparable levels of BSLB: cell interactions, differences in SV transfer are likely related to differences in the transport and shedding of cellular membranes both within and towards the cell-BSLB interface. As expected, we observed a differential inhibition in the transfer of TCR^+, $CD40L^+$, $BST2^+$ and $CD63^+$ SV to BSLB suggesting that heterogeneity results from the output of different organelles at the synapse and the active participation of several cell machineries required for transport, sorting, and neogenesis of vesicles rather than the simple rupture of cells. As expected, inhibitors affecting global organelle vesicle mobilisation including exocytosis and the trafficking of proteins from ER to PM [14, 15], as well as the mobilisation

of signalling microclusters, globally impaired SV biogenesis. The transfer of TCR^+ SV was promoted by acute dynamin inhibition (dynasore), and conversely, strongly reduced by inhibition of actin dynamics (cytochalasin D), and in lesser extent by the acute inhibition of the ESCRT machinery (MG132 and manumycin) and neutral sphingomyelinases (N-SMases by altenusin; Fig. S3C and Table S2). The increased TCR transfer observed with dynasore might result from increased ubiquitination of the antigen receptor mimicking as shown for EGFR [16]. The transfer of $CD40L^+$ SV was strongly reduced following acute inhibition of several machineries in the hierarchy ER-Golgi-PM (brefeldin A -BFA), actin dynamics and ESCRT> ceramide synthesis>dynamin>vacuolar H^+-ATPases (bafilomycin) and class I and II PI3K (effect observed with wortmannin, but not with SAR405) (Fig S3D). Other members of the TNF superfamily, such as FasL, has been also reported to be affected by BFA [17, 18], suggesting a conserved mechanism of TNFSF delivery using SV. Remarkably, consistent with their spatial segregation from CD40L, the transfer of $BST2^+$ and $CD63^+$ SVs does not require acute transport from Golgi cisternae and is mostly affected by the inhibition of endosomal and lysosomal transport dependent on N-SMases and vacuolar H^+-ATPases [19] (Fig. S3E-F). By halting the proteasome, MG132 depletes free-monoubiquitin [20] and impairs the function of ESCRT components, such as TSG101, which requires ubiquitination of cargo for transport [2, 21] (see also Fig. 5). CD40L>TCR>BST2 showed a higher sensitivity than $CD63^+$ SV to the inhibition provided by MG132, suggesting a kinetically segregated budding mechanism (i.e., multivesicular stores), unlikely to be affected by acute inhibition. The significant reduction of $CD40L^+$ and $CD63^+$ SV transfer following N-SMases inhibition by altenusin likely result from the interference with wider membrane trafficking events involving both the ER-Golgi and endosomal compartments, where N-SMases preferentially locate to regulate membrane curvature and budding [22, 23]. Finally, compared to other markers the transfer of CD40L in SV required the stepwise transport of CD40L to

the PM, and from PM to SV (Fig. S3G-J). The latter was better exemplified by BFA, manumycin and CytD (Fig. S3D and S3H), while BFA and manumycin halted transfer by reducing the upregulation of CD40L on the surface of stimulated T cells, CytD affected CD40L sorting into SV despite its significant surface upregulation, suggesting that an impaired actin-dependent mobilisation of CD40L microclusters precluded their incorporation into SV.

BSLB reveal conserved and T cell subset-specific effectors shed in SV.

Next, we sought to evaluate whether different human T cells, including $CD8^+$ cytotoxic T cells (CTL), $CD4^+$ T helper cells (TH) and cultures enriched in $CD127^{low}CD25^{high}$ $FoxP3^+$ cells (Treg) displayed distinctive SV transfer hallmarks. All cells were isolated from peripheral blood, activated, and further expanded *ex vivo* as detailed in Methods (see Fig. S4A-C). We evaluated the transfer of the TCRαβ heterodimer, CD2, the coreceptors CD4 or CD8, CD28, CD45, the SV proteins CD63 (LAMP-3), CD81 and BST2, and effectors including regulatory enzymes (CD38, CD39 and CD73), helper (CD40L) and cytotoxic (Perforin) proteins. Analyses were focused on the geometric means of the population of single T cells and single BSLB after gentle dissociation of conjugates (Fig. 2A). A normalised synaptic transfer metric was defined as the percent enrichment of T cell proteins on single BSLB from the total mean signal observed in single BSLB and single cells ($NST\% = BSLB_{GMFI}/(BSLB_{GMFI} + Cells_{GMFI}) \times 100$)[2]).

Because we used anti-CD3ε-Fab we expected no engagement of the TCR co-receptors CD4 and CD8, and therefore, the vesicular shedding of TCR with limited co-receptors shedding. Compared with TH, CTLs transferred significantly more TCR and CD8 in the range of physiological anti-CD3ε-Fab densities and consistently showed smaller EC_{50} values of 251.2 for TCR (compared to 1251 in $CD4^+$) and 50.87 for the coreceptor (compared to

56.44 in $CD4^+$) (Fig. 2B). The latter might relate with the known higher sensitivity to antigen of CTL compared to TH and might relate to an increased physical proximity and association between TCR and CD8 [24], which might promote its sorting into SV. Similarly, using chimeric antigen-receptor expressing T cells (CART), we observed a significantly higher transfer of the CAR than TCR at comparable densities of anti-CD3ε-Fab and agonistic pHLA-A*02: NY-ESO-$1_{157-165}$ complexes (Fig. S4D). CART also transferred higher amounts of CD8, suggesting that CAR triggering promotes efficient release of vesicular proteins even at low densities of antigen (Fig. S4E). Like co-receptors, and despite their high level of cell surface expression, we observed a lack of enrichment for CD2, CD28 and CD45 common to all the T cell subsets tested (Fig. 2C-F). While CD45 is normally excluded from the cSMAC and the synaptic cleft, the co-receptors CD2 and CD28 require binding to cognate ligands to be mobilised as microclusters to the synapse centre [25]. Thus, SV heterogeneity is partly defined by APC ligands dynamically feeding information to T cells. Considering the limited enrichment of CD4, CD8 and CD45 in SV, we therefore used them as secondary parameters in the discrimination of singlets in FCM analyses and sorting (Fig. S1A, Fig.S4, Fig. S6A).

TH, CTL and Treg transferred comparable levels of $CD63^+$, $CD81^+$, and $BST2^+$ SV to BSLB (Fig. 2G-I), indicating conserved mechanisms delivering these components to the synaptic cleft. Using CART, we observed that the release of $CD63^+$ SV was higher in cells stimulated via the CAR as compared to the TCR (Fig. S4F). We next measured the transfer of effector ectoenzymes, namely the ADP-ribosyl cyclase CD38 and the AMP- and adenosine-producing ectonucleotidases CD39 and CD73, as part of SV (Fig. 2J-L). While CD38 polarises to the IS[26] and participates in the generation of T-dependent humoral immunity[27], CD39 and CD73 have been suggested as tolerogenic mediators[28-30]. TH and CTL showed a limited, conserved, and comparable transfer of $CD38^+$ SV to BSLB (Fig. 2J). Similarly, we observed a discrete transfer of CD39 from Treg (Tmax = 17.83%) and TH

(Tmax = 6.5%; Fig. 2K), and a significantly greater transfer of CD73 from Treg (Tmax = 5.73 %) compared to TH (Tmax = 1.9%; Fig. 2L), which associated with a higher central clustering of CD39 and CD73 in Treg synapses (Fig. S4J-K). The inclusion of itinerant enzymes such as CD38, CD39 and CD73 in SV, although limited, might exert a feed-forward regulatory effect as shown for tumor-derived exosomes[31].

We also compared the dynamics CD40L and perforin transfer, two major effectors mediating the activation and killing of APCs, respectively. Upon TCR triggering, we observed a conserved relative transfer of CD40L in T cells, with TH secreting the most (Fig. 2M, see also Fig. 3). On the other hand, compared to TH, CTLs showed a reduced threshold for Perforin release, which was transferred to BSLB at α-CD3ε-Fab densities as low as 8 molec./μm^2 for CD8$^+$ T cells (Fig. 2N). In CART cells, perforin release followed a different behaviour than exocytic CD63$^+$ SV. More specifically, TCR-elicited perforin deposition on BSLB was significantly higher than that resulting from CAR-triggering (Fig. S5D), suggesting differential mechanisms influencing SV and SMAP release at the IS. Altogether, our data suggest that 1) T cells display differential dynamics of SV transfer consistent with their effector functions and receptor-ligand interactions occurring at the IS, and that 2) BSLB are excellent tools to study the biogenesis of both SV and perforin-containing SMAPs.

T cell activation, phenotype, *trans* presented immunoreceptors and proteolysis by ADAM10 are major determinants of SV composition: the example of CD40L.

In the dynamic exchange of information between T cells and APCs several factors might influence the effector cargo of SVs. Hence, we harnessed BSLB to study the dynamics influencing CD40L$^+$ SV release under near physiological conditions and using absolute quantifications (please refer to Methods). Absolute measurements offer a better comparison when varying CD40L expression levels exist among different T cell subsets (e.g., Fig. 2M).

First, we measured $CD40L^+$ SV release in response to CD40 densities present in different primary human B cell subsets (minimal and maximum values of 16 and 646 molec./μm^2; Fig. 3A). BSLB covering a range of 0 to 540 molec./μm^2 of CD40 were used to compare the SV transfer dynamics to BSLB between previously activated (and expanded) TH blasts, and freshly isolated (quiescent) TH. As shown in Fig. 3B, while quiescent TH transferred negligible amounts of CD40L, activated TH showed a high sensitivity to CD40, transferring CD40L to CD40 densities as low as 2 molec./μm^2. This high efficiency, however, reached maximum CD40L transfer (T_{max}) at around 20 molec./μm^2 of CD40, which at higher densities outcompeted the anti-CD40L detection antibody [2]. The latter is expected as CD40 displays a high affinity for its ligand (0.5-7.13 nM [32]). Therefore, we used the physiological minimum of CD40 (20 molec. /μm^2) to study the dynamics affecting CD40L sorting in SV. Using as vesicle stamp area of 0.84 μm^2 [2] to compare the effective density of CD40L reached on the surface of BSLB over time (Fig. 3C). After 4h, no significant transfer of vesicular CD40L was observed from quiescent cells, whereas a significant transfer of CD40L led to densities up to 1000 times to those found on the TH PM, suggesting a significant gain in CD40L binding avidity resulting from its vesicular packing. Remarkably, higher $CD40L^+$ SV transfer in activated cells related with their higher expression of TSG101 (Fig. 3D), indicating that T cell activation leads to the simultaneous up-regulation of effectors and ESCRT components. The further comparison of TH, Treg and CTL revealed phenotype-specific differences in the dynamics of CD40L transfer among activated T cells, with the amounts released in the order TH>Treg>CTL (Fig. 3E). As in Fig. 2L, TH showed an increased sensitivity for CD40L released compared to Treg and CTL (F-test, $p<0.0001$).

Next, we addressed whether TCR:pMHC binding potency influences the release of $CD40L^+$ SV. We used 3 TH clones specific for the same influenza H3 hemagglutinin peptide $HA_{338-355}$ (NVPEKQTRGIFGAIAGFI) but displaying different TCR:pMHC potencies as

determined by an IFN-γ release assay (Table S3). T cell clones showed comparable levels of CD40L transfer at higher antigenic HLA densities and formed morphologically similar synapses (Fig. 3D-E). However, contrary to their IFN-γ response, clones showed differences in the EC_{50} for CD40L transfer with clone 40 displaying the lowest (P=0.0002, EC_{50}= 22.02, compared to 66.01 and 101.9 for clones 16 and 35, respectively; Table S3), suggesting that TCR: pMHC affinity has stronger effects on the release of $CD40L^+$ SV mostly at lower antigen densities. The latter phenomenon might underpin the maintenance of an active CD40L-CD40 pathway in autoimmune diseases, where high densities of self-antigens might suffice to trigger the release of $CD40L^+$ SV despite low affinities of TCR for self-peptides and the assembly of non-canonical immune synapses [33].

Beyond antigens (signal one), APCs also present membrane-bound accessory signals (signal two) to fine-tune the activation of engaged T cells. Because the influence of accessory molecules on the vesicular output of the synapse is not fully understood, we next sought to evaluate the effects of different known T cell costimulatory and corepressing signals on the shedding of $CD40L^+$ and other SVs. We incorporated costimulatory signals including CD80, CD86, ICOSL and CD58, the latter of which forms a distal domain boosting TCR signalling known as CD2 corolla [34]. We also included the negative regulators PD-L1 and PD-L2, as well as other members of TNF ligand superfamily (TNFSF), including OX40L and 4-1BBL, whose interplay with the CD40-CD40L dyad remains poorly characterised. To evaluate whether the synaptic output of T cells could be also affected by foreign proteins, such as those participating in virological synapses, we included the HIV-1 gp120 protein, which is a known high affinity ligand for CD4 [5, 6, 35, 36]. We then compared the differences in NST% between different BSLB compositions using those containing only ICAM1, CD40 and a titration of α-CD3ε-Fab as controls (Fig. 3H-P). While CD58 incorporation slightly promoted transfer of CD2 (Fig. 3I), incorporation of CD80, CD86 and ICOSL induced an

increased synaptic transfer of CD28 (Fig. 3J). Costimulatory ligands such as CD80, CD86, ICOSL and CD58 instigated a higher, but not significant transfer of CD40L. Most remarkably, inclusion of PD-L1 and PD-L2 on BSLB resulted in a significant reduction in the transfer of $CD40L^+$ SV (Fig. 3M), and although not significant, also led to a lesser release of TCR^+, $CD28^+$, $CD63^+$, $CD81^+$, and $BST2^+$ SV. Similarly, BSLB loaded with a combination of 4-1BBL and OX40L impaired the transfer of vesicular TCR, CD81, CD40L, and BST2 from TH(Fig. 3H, L-N). Whether these differences relate with the competitive occupancy of intracellular signalling adaptors shared between CD40L, OX40 and 4-1BB is subject of further investigation. BSLB loaded with the HIV-1 gp120 instigated a reduced transfer of TCR^+, $CD63^+$ and $CD81^+$ SV at high α-CD3ε Fab without significantly affecting the transfer of $CD40L^+$ SV (Fig. 3H, K-M). Importantly, gp120 promoted CD4 transfer to BSLB (Fig. 3P) even in the absence of TCR triggering. CD4 transfer might be supported by TCR-like signalling events involving Src, Lck and CD3ζ phosphorylation as previously shown [6]. The gp120-induced transfer of CD4 and the CD58-instigated transfer of CD28 provide further evidence linking ligand binding with the sorting of proteins in SV. Altogether these data provide proof of concept that as synthetic APC, BSLBs facilitate the study of cognate and non-native molecular interactions occurring at the cell: bead interface and shaping the composition of T cell SV.

Next, we used CRISPR/Cas9 genome editing to test the functional relevance of endogenous elements participating in SV biogenesis and the inclusion of CD40L. Because we used anti-CD3 Fab for the HLA-independent triggering of TCR, we expected negligible participation of CD4 in SV biogenesis, and hence, selected a guide RNA (gRNA) producing limited downregulation of the coreceptor (67.83 ± 10% of baseline) as a control. We also selected gRNAs targeting membrane structural proteins (*BST2*, *CD81*), and the ESCRT-I component *TSG101*, which participates in the budding of synaptic ectosomes [2]. We also

targeted ADAM10, a disintegrin and metalloproteinase mediating the shedding of surface FasL and CD40L from activated T cells [37, 38], as might mediate CD40-induced transfer of soluble CD40L ectodomains [39]. A significant downregulation of the relevant targets was observed on the surface of cells edited for BST2 (45.08 ± 23.19% of baseline), CD81 (7.63 ± 4.8%) and ADAM10 (9.37 ± 2.83%), the latter of which led to a significant upregulation of CD40L at the cell surface (224.2 ± 114.8%) (Fig. S5A-D).

As with inhibitors, we compared SV transfer in terms of the T_{max} % observed in controls (*CD4*-gRNA). While ADAM10 downregulation increased both the cell surface expression and the transfer of $CD40L^+$ SV to BSLB, the downregulation of CD81, BST2 and TSG101 reduced the transfer of $CD40L^+$ SV without significant downregulation of CD40L at the PM (Fig. 4A and S5A-B). As expected, *CD81* and *BST2*-edited cells showed significant reduction in the transfer of their respective $CD81^+$ and $BST2^+$ SV (Fig. 4D-E, respectively), and non-significant differences with regards to other markers (Fig. 4B-E). *TSG101* editing led to a significant reduction of $CD40L^+$ and TCR^+ SV transfer without affecting their baseline surface expression levels, indicating a bona-fide inhibition of their vesicular sorting dependent on ESCRT (Fig. 4A-B). Remarkably, *TSG101* downregulation partly phenocopied the effects of monoubiquitin depletion by MG132, with inhibition of transfer affecting mostly $CD40L^+$ SV, and to a lesser extent TCR^+ SV (Fig. 2C-D). Remarkably, $CD63^+$ SV transfer was less affected by downregulation of *CD81*, *ADAM10*, *BST2* and *TSG101* (Fig. 4C), providing an additional piece of evidence for CD63 vesicular transfer relating mostly to the transport and exocytosis of preformed MVB or lysosomal cargo, which is also congruent with our observations with the panel of inhibitors. Imaging of synapses formed on glass SLB further revealed that reduced transfer to BSLB correlated with a significant central clustering and overall polarisation of CD40L to the interface formed between *CD81*-, *BST2*- and *TSG101*-edited cells and SLB (Fig. 4F-G). ADAM10-edited cells on the other hand, showed

an increase in the average amount of polarised CD40L and more importantly, a significant increase in total CD40L clustered within contacts (Fig. S5E). Congruently, we observed a reduced T_{max} of $CD40L^+$ SV for *CD81*-, *BST2*-, and *TSG101*-edited cells, the latter of which also displayed a reduced T_{max} for TCR^+ SV (Fig. S5F-I) and a reduced mobilisation of CD40L to the cell surface upon TCR-triggering (Fig. S5J). Expectedly, ADAM10-edited cells showed increased T_{max} and reduced EC_{50} for the release of $CD40L^+$ SV, and a marked cell surface upregulation of CD40L following TCR triggering (Fig. S5I and J, respectively). The partial reduction in CD40L transfer following downregulation of CD81 and BST2, suggests that these membrane integral proteins work as aiding factors in the release of $CD40L^+$, but not TCR^+ nor $CD63^+$ SV. Also, the differential requirement for TSG101 among TCR^+, $CD40L^+$ and $CD63^+$ SV, which is phenocopied by MG132, suggest that different cellular machineries might underpin SV heterogeneity. The increased transfer of $CD40L^+$ SV from ADAM10-deficient cells also suggests a minimal participation of cleaved ectodomains on the transferred pool of CD40L.

RNAseq of BSLB reveals the higher specialisation of SV in the transfer of miR and RBPs.

Within the framework of harnessing BSLB for the study of effectors released at the IS, we then sought to identify miR species associated with SV. To minimize cell contamination, we isolated BSLB coated with TCR^+ SV using fluorescence-activated cell sorting of single beads after 90 min of culture with T cells (Fig. S6A), followed by small RNA purification. Small RNAs were also purified from syngeneic sEVs as controls. Analyses of SV and sEV libraries raw reads revealed a similar composition of small RNA species, of which miR were overall more enriched in SV than sEV and the parental cells (Fig. 5A). After identifying small RNA species conserved across samples, donors, and sequencing

runs, GSEA further revealed that the majority of enriched miRs were shared between SV and sEV for both TH and CTL. However, from 200 miR species enriched in TH, 11 were uniquely enriched in SV and 23 in sEV, whereas from 163 miR species enriched in CTL, 17 were unique to SV and 19 to sEV (Fig. 5B and Table S6). Consistent with the higher variety of enriched miR in sEV, we observed a higher variance compared to SV (Fig. 5C). Further analyses of enriched motifs with MEME [40] mapped enriched motif to unique and shared miR species in TH (Fig. 5D) and CTL (Fig. 5E), which together redundantly associated to GO pathways related to immune cell signalling and anti-tumor immunity (Fig. 5F and heatmaps in Fig. S6B). Congruently, miR target enrichment analyses of enriched miR further revealed a similar degree of redundancy in the mapped targets (see Table S7 for the full list of targets and Fig. S6C-H for GO terms), which included RNA-binding proteins, such as DICER, AGO1/2, TNRC6A/B, PLAGL2, and RRM2; immune receptor adaptors and signalling proteins such as CD2AP, IFNARs, SMADs; and synaptic ligands and effectors including ICAM1 and trombospondin-1 (THBS1), among others.

Although sEV showed slightly more enriched miRs, the overall enrichment of these small RNA species was higher in SV suggesting a higher association of these vesicles with miRs and their functional proteins. Supporting this notion, LC-MS/MS analyses comparing SV and sEV showed an overall increasing enrichment of nucleic acid-binding proteins, including several interacting with RNAs (Fig. S7A-B, noise subtracted and normalised). SV also displayed reduced levels of ADAM10 and of contaminants, including Histone 3, LGALS3BP[41] and RNAse 4 (Fig. S7C). The targets of some enriched miRs (GBR2 in Fig.S7D and Table S7) were also detected. Remarkably, GSEA using PANTHER revealed an enrichment of GO terms relating to global RNA-binding and RNA-interference in SV (Fig. S7E). Consistent with the unbiased identification of the RBPs YBX1 and SF3B3 in SV (this work) and SE [2], we found their polarisation and localisation as discrete puncta in the

synaptic cleft (Fig. S7F-H, white arrows). Similarly, the polarisation of ER-like structures together with the detection of ceramide and RNA puncta both in vesicular tracks of cells resuming migration and in the synaptic cleft (Fig. S7I-J, yellow arrows) further supports the active delivery of vesicular RNA within the IS. The localisation in the synaptic cleft of YBX1, a known protein packing small non-coding RNAs in EVs [42, 43], suggests the delivery of ribonucleoprotein complexes in SV. Altogether these data suggest that SV serve as platforms for the dedicated delivery of both immune receptors and ribonucleoprotein complexes comprising small non-coding RNAs and their functional partners. Interestingly, we also found the enrichment of GO terms related to telomeric DNA binding in SV (Fig. S7E), which suggest that telomere binding proteins are polarized at the IS of T cells to facilitate telomere exchange as recently shown for APCs [44].

The second layer of information provided by transferred miR and their protein partners might be pivotal for the functional modulation of APCs in the narrow space-time of the IS. Beyond the effects expected on opposing cells, the release of miRs associated with SV might work as a potential regulatory mechanism finely tuning T cell activation and effector function by providing a hub for the elimination of suppressor miRs.

DISCUSSION

The first observation of T cells being successfully activated by bead supported bilayers presenting antigenic MHC-II dates back to 1986 [45]. Others have demonstrated the versatility of BSLB as APCs in several experimental contexts, including measuring the dimensions of interfacial receptor-ligand interactions, as well as the localisation of lipid species and CD3ε in the pole of T cells interacting with agonists BSLBs [46, 47]. Here we leveraged the APC capabilities of BSLB to isolate and study in more detail the composition and biogenesis of T-cell shed EVs. Most importantly, BSLB facilitated for the first time the

comparison of SV and sEVs, providing evidence for highly heterogeneous, yet unique populations of vesicles being released in the limited dwell-time of the IS. Quantitative differences in size, protein loads and association to miR and RBPs between SV and sEV were corroborated.

The acute pharmacological inhibition and CRISPR/Cas9-edition of TH strongly indicated that mechanistically SV heterogeneity is partly explained by contributions of several cellular machineries recruited at the interacting pole of activated T cells. We provide evidence for an overarching hierarchy in the mechanisms participating in the vesicular transfer of CD40L with the dominant participation of ER/trans-Golgi transport and the ESCRT machinery, and the secondary participation of multivesicular bodies and lysosomes. The selective increase transfer of TCR^+ SV resulting from dynamin inhibition, and the less dramatic effect of ESCRT-inhibition/downregulation on $CD63^+$ SV transfer provide additional evidence for different sorting mechanisms participating in the biogenesis of SV (Fig. S3C-F and Fig.5). We provide evidence for a critical role of ADAM10, a protease known to be active at the PM, in regulating the pool of surface CD40L and the resulting levels of $CD40L^+$ SV shedding dependent on CD40. Interestingly, our LC-MS/MS analyses indicate that compared to SV, sEV incorporate a higher amount of ADAM10 (Fig. S7C) providing an explanation for the increased expression of CD40L on SV (see Fig. 1I).

Microvilli have been recently shown to lead to the formation of effector membranous particles referred to as synaptosomes, which are enriched in LFA-1, CD2 and cytokines [48]. Microvilli tips are known to accumulate proteins including TCR, CD2, and CD4 [48, 49]. Here we show that T cells transfer little vesicular CD2 and CD4 (Fig.1D), which increased only and at limited levels upon ligation by CD58 and HIV-1 gp120, respectively (Fig. 2C-D, 3I and 3P). Also, TCR signalling, which is required for SV biogenesis, is also known to

produce microvilli disassembly [49], suggesting that synaptosomes, which are different in origin and structure to ectosomes, contribute minimally to the vesicular output of the IS.

SV biogenesis is a highly tailorable and dynamic process connecting the integration of signals presented by APCs with the particulate output of activated T cells. Earlier electron microscopy studies demonstrated budding of TCR^+ ectosomes with partial polarisation of MVB and trans-Golgi in stimulated cells (figure 1C in ref[1]). In these experimental settings, SLB lacked CD40, which as we later demonstrated promotes the quick mobilisation of CD40L to the PM, microclusters and budding ectosomes [2]. Here we provide evidence that shedding of $CD40L^+$ SV not only requires CD40 on presenting BSLBs, but also its quick mobilisation from ER-Golgi stores. Beyond CD40, we provide evidence of other signals finely tuning SV heterogeneity, including B7 receptors (CD80/86), PD-1 ligands, other TNFSF members and non-native ligands. For instance, HIV-1 gp120 promoted the vesicular transfer of CD4 and CD40L at low, physiological densities of α-CD3ε Fab. Similarly, the non-native interaction between CARs and antigenic HLA complexes led to a remarkably efficient transfer of CAR as part of SV and at the expense of its cell surface expression levels (Fig. S4D, red arrow). The superior vesicular shedding of CAR containing CD3ζ signalling tails might result from rewired TCR signalling networks and the formation of multiple, short lived synapses [50]. Since reduced CAR expression might desensitise CART to new encounters with target cells, understanding the mechanisms underlying the supraphysiological shedding of CARs is necessary to increase the therapeutic effectiveness of adoptive T cell therapies.

The sequencing of BSLBs made possible the first side-by-side comparison of the miR cargo associated to SV and sEV. We found that both miRs and RBPs were significantly more enriched in SV than sEV (Fig. 5A and S7E). Different from immune receptors, which require gains in avidity to feed-forward activation signals to APCs, miRs might rely on redundancy

to exert functional modulation. In other words, the high level of target redundancy found in the enriched miRs of both SV and sEV provides an alternative mechanism supporting the effector role of miRs, especially in conditions in which scarce copies of single species are transferred associated to EVs [51]. In addition, the transfer of miRs as functional ribonucleoprotein complexes might promote their effector function across short-lived cellular contacts. Supporting this hypothesis, we found RBPs enriched in LC-MS/MS of SV and SE, namely YBX1 and SF3B3, in the synaptic cleft of TH. Alternatively, SV might serve as '*trash bags*' for the clearance of miR species controlling various aspects of T cell proliferation and the effector response.

The recent identification of glycoRNAs being integrated to and presented as part of the cellular glycocalyx [52] suggests that miR species might be transferred alongside immune receptors in the surface of SV, especially synaptic ectosomes. Together with the high enrichment of miR in T cell SV, we have provided evidence for the shedding of highly glycosylated vesicles in the synaptic cleft ([2] and Figs. 3G, S2G-H, S4K, see WGA puncta). Furthermore, the high molecular heterogeneity of SV should be considered when reconstituting systems pursuing the delivery of specific miRs [53]. Signals derived from effector immune receptors might direct the fate of internalised miR^+ SVs in acceptors cells and the efficiency of their functional modulation.

The intrinsic feed-forward function of SV-enriched immune receptors and miRs, specifically and timely released in response to antigen is different in kind and structure to other signals integrated early during T cell activation. Therefore, we consider that the heterogeneity and effector diversity of the particulate output of T-cell synapses, including SV and SMAPs, deserves its own functional classification as signal four. We expect BSLB will help others in the high throughput study of other key factors driving signal four-dependent communications. Undoubtedly, the comparison of sEVs and SV in other immune cells known

to secrete highly heterogeneous EVs, such as DCs[54], or in cells using similar interfacial communications (e.g., platelets upregulating CD40L and stromal cells secreting ADAM10 inhibitors) are needed to elucidate whether SVs are key information units of cellular networks.

FIGURE LEGENDS

Figure 1. As synthetic APC, Bead-Supported Lipid Bilayers (BSLB) trigger synapse formation and the release of synaptic vesicles by stimulated T cells. (A) fluorescence correlation spectroscopy of α-CD3ε Fab AF488 and lipid (ASR-PE) diffusion on BSLBs at 37^{o}C. (B) Representative time-lapse confocal microscopy showing the interaction between TH and BSLB and the active transfer of CD40L^{+} synaptic stamps to BSLB (white arrowheads), which are left behind after the interaction resolves. (C) Imaging FCM showing the transfer of different T cell proteins as stamp on the surface of BSLB, including TCR, CD81, CD38 and CD4. *Bottom:* an example of BSLB showing a discrete distribution of ICAM-1 and vesicular proteins (see also Fig. S1B-C). (D) Histograms showing the transfer of TH (violet histograms) proteins to BSLB (blue histograms) presenting increasing densities of α-CD3ε Fab and 200 molec./μm^2 of ICAM1 and 20 molec./μm^2 of CD40. (E-F) After conjugate separation by cold, SV patches are released from BSLB with the use of 50 mM EDTA resulting in the release of BSLB attached TCR and CD40L (F) as measured by FCM staining. (G) Transmitted electron microscopy of eluates reveals the presence of extracellular vesicles and small soluble proteins. Scale bar= 200 nm. (H-K) NanoFCM analyses of TCR (H), CD40L (I), and CD63 (J) median fluorescence intensity (normalised to isotype). Steadily shed EVs (sEV) were isolated by differential centrifugation of cell-free culture supernatants. Synaptic Vesicles (SV) were eluted from BSLB after conjugate dissociation and isolated by

differential centrifugation. Normality was determined using Shapiro-Wilk test and statistical significance was determined by two-tailed unpaired t-test (F, H-J). *p≤0.05, **p≤0.005, ***p≤0.0005, ****p≤0.0001 and ns = not significant. Data representative of n=3 to 5 independent experiments (B, D-I). In I, CD40L signal might be underestimated in SV by the presence of eluted CD40 and its competition with labelling anti-CD40L (see also Figs. 3B and S2I). (K) Left: Representative half overlaid histograms of SV stained with either isotype control or antibodies against TCRαβ, CD40L and BST2. Right: Overlaid histograms showing size-calibration beads (top grey, numbers represent nm in diameter) for the interpolation of vesicle median sizes; TCR^+ sEV (yellow) and SV (blue) are shown.

Figure 2. The synaptic transfer of vesicular effectors relates to the functional properties of different T cell subsets. (A) Gating strategy for the selection of single BSLB and T cells for the measurement of the transfer of vesicular effector at the IS. BSLBs presenting α-CD3ε Fab (0 to 1,000 molec./μm^2), 200 molec./μm^2 of ICAM1 and 20 molec./μm^2 of CD40 were used in all experiments. (B-L) Percent Normalized Synaptic Transfer (NST= [$cGMFI_{BSLB}$/($cGMFI_{BSLB}$ + $cGMFI_{Cells}$)]*100) to BSLB from TH (green), Treg (blue) and CTL (violet). Ligands included (B) TCR; (C) CD2; (D) TCR co-receptors (CD4 or CD8); (E) CD28; (F) CD45; (G) CD63; (H) CD81; (I) BST2; (J) CD38, (K) CD39; (L) CD73, and (M) CD40L. (N) Perforin transfer as background subtracted GMFI is shown. Representative histograms for most makers are shown on the right for TH (green) and CTL (violet). Statistical significance was determined by multiple t-test comparing SV transfer across different α-CD3ε Fab densities and among different T cell populations. EC_{50} and transfer maximum (Tmax) were determined using F-test and three to four parameters fitting (H-J). *p≤0.05, **p≤0.005, ***p≤0.0005, ****p≤0.0001 and ns = not significant. Data represent means ± SEM of n=4-10 independent experiments.

Figure 3. Harnessing BSLBs to dissect the dynamics influencing the biogenesis of CD40L$^+$ SV. (A) CD40 densities on the surface of human B cells isolated from either peripheral blood (CD19^{hi} HLA-DR$^+$ and CD40$^+$) or palatine tonsils (also CXCR5^{hi}). (B) Based on data in A, BSLB were reconstituted with increasing densities of human CD40 and analysed for their capacity to instigate the release of CD40L$^+$ SV. Quiescent and α-CD3/CD28-activated TH are compared. BSLB presenting either no α-CD3ε or 1,000 molec./μm^2 were used in these experiments. (C) As in B, TH cells were incubated for 4h with BSLB and the density of CD40L compared to 1 h activated TH controls. (D) TSG101 expression by flow cytometry (left) and immunoblotting in quiescent and activated TH. (E and F) Comparison of CD40L$^+$ SV transfer among different T cell types (*green:* TH; *blue:* Treg-enriched; *violet:* CTL), and among T cell clones (E) specific to the influenza H3 HA$_{338-355}$ peptide presented in HLA-DRB1*09:01. (G) TIRFM images showing CD40L clustering within the synapses of T cell clones stimulated on SLB containing 30 molec./μm^2 of antigen, 200 molec./μm^2 of ICAM1 and 20 molec./μm^2 of CD40. Scale bar = 5 μm (A-H) After cell: BSLB conjugate dissociation FCM measurement was performed on BSLB to calculate the normalized synaptic transfer (NST%) of SV positive for (H) TCR, (I) CD2, (J) CD28, (K) CD63, (L) CD81, (M) CD40L and (N) BST2 was measured on control (green) or BSLB presenting CD80, CD86, ICOSL (blue), CD58 (red), PD-L1 and PD-L2 (magenta), HIV-1 gp120 (grey), and OX40L and 4-1BBL (black) (all at 100 molec./μm^2). (O) Representative half-overlaid histograms showing CD40L$^+$ SV transfer to ligand- and α-CD3ε-Fab-coated BSLB. Control BSLB were tailored to present ICAM1, CD40 and titrations of α-CD3ε-Fab. (P) NST% of CD4 to control (green) and HIV-1 gp120-presenting BSLBs (grey; red arrows indicate the loss of CD4 on TH). Normality was determined using Shapiro-Wilk test and statistical significance was determined by multiple t-test to compare levels of CD40L$^+$ SV

transfer to BSLB across different CD40 densities, times, T cell populations (B-C, E-F), and increasing antigen densities (either α-CD3ε Fab or HLA-DRB1*09:01:HA complexes). EC_{50} and transfer maximum (T_{max}) were calculated using three to four parameters F-test (E, F). In D, Wilcoxon matched pairs signed rank test. *P* = 0.0312 was used to compare TSG101 expression between quiescent and activated cells. In H-P, multiple t-test comparing control BSLB presenting 200 molec./μm^2 of ICAM1, 20 molec./μm^2 of CD40 and α-CD3ε Fab (0 to 2,000 molec./μm^2) with BSLB also presenting the selected group of proteins each at 100 molec./μm^2. *p≤0.05, **p≤0.005, ***p≤0.0005, ****p≤0.0001 and ns = not significant. Data represents means ± SEM of n=4 (A-E and H-P) and n=3 (F, G) independent experiments.

Figure 4. Harnessing BSLBs to identify key proteins participating in the biogenesis of CD40L$^+$ SV. (A-E) Data showing the transfer of SV as measure by flow cytometry of BSLB after the dissociation of cell:BSLB conjugates. We used a normalised transfer metric expressed as the percent of the transfer max (T_{max}) observed in *CD4*-edited controls. Heatmaps show T_{max}% for different SV populations, including those positive for (A) CD40L, (B) TCR, (C) CD63, (D) CD81 and (E) BST2 on BSLB incubated with different CRISPR/Cas9-edited cells (targets shown in italic). Normality was determined using Shapiro-Wilk test and statistical significance was determined by multiple t-test corrected for multiple comparisons (Holm-Sidak) and comparing SV transfer to BSLB between CRISPR/Cas9 edited cells and *CD4*-edited controls (and depicted as % of its T_{max}). BSLB contained 200 molec./μm^2 of ICAM-1, 20 molec./μm^2 of CD40 and four increasing densities of anti-CD3ε Fab (0-2,000 molec./μm^2). (F-G) The degree of CD40L central clustering and synaptic release was measured in different CRISPR/Cas9-genome edited cells. (F) CD40L Mean Fluorescence Intensity (MFI) in immunological synapses of CRISPR/Cas9-edited cells. (G)

Representative TIRFM images showing mature immunological synapses and the levels of centrally clustered CD40L. *p≤0.05, **p≤0.005, ***p≤0.0005, ****p≤0.0001 and ns = not significant. Data representative of n=6 (A-E) and 4 (F-G) independent experiments.

Figure 5: SV are enriched in miR, which include both unique and public species with considerable functional redundancy to sEV. (A) Abundance of different genome-mapped RNA species found associated to SV, syngeneic sEV, and parental cells. (B) Counts of enriched miR species associated to SV, sEV and parental cells (see also Table S6). (C) miR heterogeneity is further reflected by PCA of the analysed EV subpopulations. (D) Motif analyses using MEME identified consensus sequences (central inserts) mapped across different miRs for TH SV (top panel) and TH sEV (bottom panel). (E) Motif analyses using MEME identified consensus sequences (central inserts) across different miRs for CTL SV (top panel) and CTL sEV (bottom panel). (F) Bar graph displaying the number of miR species enriched uniquely in SV (violet), uniquely in sEV (green), or shared (grey). TH miR targets are shown in the top panel, and CTL miR targets are shown in the bottom panel. Data representative of at least six independent experiments, samples with low RNA yields were pooled for sequencing (n = 8 donors).

Supplementary Figure 1; related to Fig. 1. Multiparametric analyses of shed SV shows a highly heterogeneous population of vesicles being transferred at the IS. (A) T cell: BSLB synapses and the release of synaptic ectosomes containing engaged T cell molecules can be studied by conventional multicolour flow cytometry (FCM), imaging FCM and nanoFCM. As conventional multicolour FCM (A), imaging FCM (B) facilitates the identification of BSLB and cells primarily by area (low for BSLB) and aspect ratio comparisons (high, close to 1), and secondarily by high fluorescence to Atto lipids (for BSLB). *Bottom:* Extended

depth of field (EDF) imaging FCM microphotographs showing single 5 µm BSLB derived from single event gates are shown. Greyscale fluorescence is shown for individual fluorescent channels and markers. Merged examples showing the colocalization of three and four markers as synaptic stamps (white arrowheads) are shown. (C) Colocalization analyses were performed using the plugin EzColocalization to calculate the overall Pearson's correlation coefficient of TCR and different markers on gated BSLB singlets (two transmitted light (TL) channels show single beads on the field of view in B). Data displaying means ± SEM of a total of 2,539 single BSLB. Normality was determined using Shapiro-Wilk test and statistical significance was determined by Kruskal-Wallis test corrected for multiple comparisons (Dunn's). *$p \leq 0.05$, **$p \leq 0.005$, ***$p \leq 0.0005$, ****$p \leq 0.0001$ and ns = not significant. (D) Flow cytometry measurement of the level of DOPE Atto lipid trans endocytosis in TH cocultured with BSLB presenting increasing densities of α-CD3ε Fab. Data shown is as % of the total signal in BSLB. *Bottom:* Examples of non-EDF imaging FCM showing only TH cells (lymphoblast). The white arrowheads show trans endocytosed material in gated TH cells (*top:* ICAM1 and *bottom:* DOPE Atto 565 lipids).

Supplementary Figure 2; related to Fig. 1. NTA, NanoFCM and imaging of T cell synapses indicate a high heterogeneity in size, marker expression, and spatial segregation in T cell SV released within the IS. (A) Nanoparticle Tracking Analyses (NTA) displaying size distribution of eluted synaptic vesicles (SV) from BSLB stamps, and steadily shed EVs (sEV, bottom insert). (B) Size distribution measured by NanoFCM of marker positive events and comparing sEV (yellow) with SV (blue). (C) NanoFCM analyses of eluates (top panels) between null BSLB containing ICAM1 and CD40 (left panel), and agonistic BSLB containing also α-CD3-Fab (1,000 molec./µm^2; right panel). Note that recombinant protein aggregates contribute to double negative events (see also (J)). Bottom

panels show conventional FCM of control and eluted BSLB. Levels of TCRαβ (*bottom left panel*) and CD63 (*bottom right panel*) fluorescence in non-agonistic (null) BSLB (black histograms), and α-CD3-Fab presenting BSLB after conjugate dissociation (light green and light blue histograms for TCRαβ and CD63, respectively). BSLB stained with antibody isotypes are shown in light grey, and BSLB incubated with increasing concentrations of cold EDTA are shown in shades of darker greens and blues. (D) Pearson's correlation coefficient (PCC) for the spatial colocalization between CD40L and other vesicle markers released within the cleft of TH synapses. Data shown is from TIRFM images shown in E-H and analysed in Fiji using EzColocalization [55] to calculate PCC for pixel spatial colocalization in synapses formed between cells and glass-supported planar SLB (PSLB) containing 200 molec./μm^2 of ICAM1, 20 molec./μm^2 of CD40 and 30 molec./μm^2 of α-CD3ε Fab. SIRC: surface interference reflection contrast microscopy. Glycans in the plasma membrane (PM) and SV of T cells is labelled with Wheat Germ Agglutinin (WGA). (E-H) Representative TIRFM images showing the discrete spatial distribution of CD40L and other extracellular vesicle markers including (E) CD63 (*Top:* with CD40L, and *bottom*: with negligible CD40L release); (F) CD81; (G) ADAM10 (as control); and (H) BST2. Images showing distribution of markers within the cSMAC of either mature synapses (F-H) or synapses in the process of symmetry breaking to resume migration (E). Scale bar = 5 μm. (I) Western Blot analyses of 2.5 x 10^5 cells (first lane), and the signal derived from 1.5 x 10^7 BSLB either negative for antigen but loaded with CD40 (second lane) or loaded for antigen (third lane). Arrows on the left indicate the size for membrane bound CD40L (25 kDa) and soluble CD40L (17 kDa). (J) TEM of eluates derived from null BSLB showing the presence of recombinant protein aggregates. Normality was determined using Shapiro-Wilk test and statistical significance was determined by Kruskal-Wallis test corrected for multiple comparisons (Dunn's). Data representative of n=4 (A-C) and 2 (E-J) independent experiments. In D each dot represents

the average PCC per synapse. *p≤0.05, **p≤0.005, ***p≤0.0005, ****p≤0.0001 and ns = not significant.

Supplementary Figure 3; related to Fig. 1. Output merging from different subcellular compartments underpins SV heterogeneity at the IS. TH were preincubated for 30 min with a panel of 12 inhibitors and then cocultured with control and agonist BSLB at a 1:1 ratio while keeping inhibitor concentrations. When possible, we used compounds redundantly targeting subcellular processes to elucidate effects related with the shared targets rather than to off-targets and used concentrations validated elsewhere [20, 21, 56-76] (Table S2). (A) After 90 min of culture, we measured the cell surface expression of key synaptic and SV markers, and (B) the stability of cellular contacts by tracking the percent of remaining cell: BSLB conjugates following cold incubation. BSLB presenting 200 molec./μm^2 ICAM1, 20 molec./μm^2 of CD40 and increasing densities of anti-CD3ε Fab were used in all experiments. (C-F) Transfer of TCRαβ$^+$ (C), CD40L$^+$ (D), BST2$^+$ (E), and CD63$^+$ (F) SV to BSLB compared and normalised to the maximum transfer observed in control untreated cells (i.e., maximum measured transfer (Tmax) per donor and at 2,000 molec./μm^2). Right heatmaps display *P*-values for the comparison of SV transfer between controls and inhibitors, and across different α-CD3ε-Fab densities. (G-J) Dynamics of TCRαβ (G), CD40L (H) BST2 (I) and CD63 (J) cell surface expression normalised to the baseline of untreated controls. In (J) out of range values (>200% are represented in orange). Statistical significance and *P*-values were determined using mixed-effects model ANOVA with Geisser-Greeenhouse correction for the determination of normalised protein expression across different donors (A), and multiple t-test to compare levels of conjugate formation (B), levels of %T_{max} SV transfer (C-F), and levels of normalised cell surface expression of relevant markers as % of control

baseline (100%) (G-J) across different α-CD3ε Fab densities. *p≤0.05, **p≤0.005, ***p≤0.0005, ****p≤0.0001 and ns = not significant. N=6 different donors.

Supplementary Figure 4; related to Figure 2. (A-C) Isolation and expansion of $FoxP3^{+}$-enriched $cCD4^{+}$ T cell cultures (termed herein as Treg). (A) sorting of cells on day 0 based on the high expression of CD4, negative expression of CD127 and further separation of CD25 low and the 5% highest population for CD25. Sorting purity controls are shown. Cells were then expanded for 14 days and used for experimentation between day 15 and day 17. (B) Example of intracellular staining for FoxP3 on day 15, and (C) the quantification of percent $FOXP3^{+}$ cells on day 15 of culture. (D-I) BSLB can be also tailored for the study of CART cell synaptic vesicles. Data shown in A-E represent means +/- SEM from two independent experiments evaluating the transfer of the chimeric antigen receptor (CAR) (D), the TCR co-receptor CD8(E), CD63(F), Perforin(G), and as its comparison to TCR (H). In D-H, Normality was determined using Shapiro-Wilk test and statistical significance was determined by Multiple t-test. *p≤0.05, **p≤0.005, ***p≤0.0005, ****p≤0.0001 and ns = not significant. (I) Representative pseudocolor plots showing the gating strategy for identifying single BSLB and single CART. (D-G) Representative half-overlaid histograms are shown to the right. The differences in synaptic transfer at comparable α-CD3ε and HLA-A2: NY-ESO-1 densities (140 molec./μm^2). SV transfer instigated by either the CAR antigen (top panels; teal BSLB), or the anti-CD3ε Fab (bottom panels, violet BSLB) are shown for each marker. Cells are shown in dark blue (no antigen/anti-CD3), and light blue (co-cultured with either HLA-A2: NY-ESO-1 or α-CD3ε). Light grey BSLB represent those loaded with no antigen. (J-K) Increased synaptic transfer of CD39 (J) and CD73 (K) to BSLB associates with higher central clustering of CD39 and CD73 in Treg synapses imaged by TIRFM. Left panels: TIRFM images comparing TH (top) and Treg (bottom) showing the distribution of the

ectonucleotidases (A) CD39 and (B) CD73 in mature immunological synapses. Middle panels show background subtracted mean fluorescence intensities (corrected MFI) for CD39 and CD73 in the contacts of TH and Treg cells stimulated on planar glass SLB containing 200 molec./µm^2 of ICAM1, 20 molec./µm^2 of CD40 and 30 molec./µm^2 of anti-CD3e Fab (clone UCHT-1). SIRC: surface interference reflection contrast microscopy. Plasma membrane (PM) of T cells is labelled with Wheat Germ Agglutinin (WGA). White arrowheads show released WGA$^+$ CD73$^+$ vesicles (diffraction limited). Scale bar = 5 µm. Two independent experiments are shown. Points represent individual synapses. Right panels: transfer behavior to BSLB and PSLB relates with an increased surface expression of both ectonucleotidases in Treg cells (blue) compared to TH (green). Normality was determined using Shapiro-Wilk test and statistical significance was determined by two-tailed Mann-Whitney unpaired test. *p≤0.05, **p≤0.005, ***p≤0.0005, ****p≤0.0001 and ns = not significant.

Supplementary Figure 5; related to Fig. 4. (A) Surface protein expression for TH from 9 different donors edited using CRISPR/Cas9 targeting CD4, CD81, ADAM10, BST2, and TSG101. (B) Representative half-overlaid histograms and bi-parametric contour plots showing the surface expression levels of edited proteins (headings) and its relationship with the expression of CD40L expression on cells (Y-axis). (C) Relationship between CD40L expression and CD3ξ expression *CD4*- (teal) and *ADAM10*-edited cells (orange). (D) TSG101 downregulation resulting from CRISPR/Cas9-genome editing shown normalized to beta actin (left panel). (E) Total CD40L signal clustered at the immune synapse of control (CD4-edited) and ADAM10-edited cells (see also Fig.4 F and G). (F-J) Dynamics of SV transfer between different CRISPR/Cas9 edited cells and the resulting downregulation of the markers on the cell surface. Non-linear, three parameter regression analyses (F-test) to

compare TCR^+ and $CD40L^+$ SV transfer among CRISPR-Cas9 knockdowns and in response to increasing densities of agonistic α-CD3ε-Fab. (F) Summary of T_{max} and EC_{50} metrics calculated for curves of TCR^+ and $CD40L^+$ SV transferred to BSLB (as shown in A). (G-H) Dynamics of $TCR\alpha\beta^+$ SV transfer to BSLB(G) and the resulting downregulation of TCRαβ on the surface of T cells (H). (I-J) Dynamics of $CD40L^+$ SV transfer to BSLB (I) and its resulting upregulatiom on the surface of T cells following stimulation with α-CD3ε-Fab (J).

Supplementary Figure 6; related to Fig. 5. (A) Sorting of BSLB after conjugate dissociation for the sequencing of SV small RNA. Upper panel: Pseudocolor plots showing the gating strategy for sorting single BSLB for the downstream sequencing of small RNAs. Shown are post-sorting controls. Right overlaid histograms showing TCRαβ on BSLB loaded with anti-CD3ε Fab (violet) versus null controls (grey) after sorting from T cell: BSLB cocultures. Bottom panel: post-sort control showing the enrichment of single cells. (B) KEGG GO pathway enrichment analyses reveals unique miR to both T-cell SV and sEV and sharing association with common biological processes. heatmap detailing miR species and KEGG GO pathways functionally enriched in TH SV, TH sEV, CTL SV and CTL sEV; Heatmap values represent log10 p-values. (C-F) Bubble plots depicting the target pathways functionally associated with miR identified in TH SV (C), TH sEV (D), CTL SV (E), and CTL sEV (F); circles represent different GO terms, circle size represents the number of targets associated with the given GO category, the overall colour represents the cluster (broader category) encompassing the most enriched GO categories. (G-H) Number of miR targets across different GO pathways. CTL SV and sEV (G), and TH SV and sEV (H) are compared. Shared miR targets per category are shown in grey, unique targets for SV are shown in magenta and unique targets for sEV miR are shown in green.

Supplementary Figure 7; related to Fig. 5. SV are enriched in RBPs some of which localise as discrete puncta in the synaptic cleft of mature TH immune synapses. (A-B) LC-MS/MS analyses of enriched proteins found in eluted SV (A) and syngeneic sEV (B). Eluted SV samples from α-CD3-Fab^{+} BSLB were corrected to background contaminants using the eluted material of Null BSLB prepared in parallel. Normalised LFQ values (log10) for enriched proteins (as determined by comparisons to the mean of all the samples analysed) are depicted in the heatmaps. (C) As in A-B, LC-MS/MS analyses showing the differential enrichment of TCR, CD40L (TRAP1), recombinant CD40 (eluted from BSLBs) and ADAM10 in SV compared to sEV. The limited enrichment of ADAM10 in these samples correlates with the reduced central clustering of ADAM10 in T cell synapses as shown in Fig. S2D and G. The heatmaps shows also that contaminants usually found in sEV fractions including RNAse4, Galectin 3 binding protein (LGALS3BP) and Histone 3 are not found in SV. (D) heatmaps showing the presence of miR targets in SV and sEV of TH and CTLs, respectively. (E) GSEA using PANTHER [77] reveal the superior enrichment of RBPs in the LC-MS/MS of SV (magenta) derived from TH (left bar graph) and CTL (right bar graph) as compared to syngeneic sEV. Values represent the fold enrichment of identified proteins per GO term. (F-H) TIRFM imaging of RNA binding proteins detected in (A) in the synaptic pole of T cells. After 20 minutes of stimulation on planar supported lipid bilayers, T cells were fixed, permeabilised and stained with monoclonal antibodies against vimentin for the identification of the cSMAC and pSMAC (yellow) and Y-BOX binding protein 1 (YBX1; white arrows indicate its localisation in the vesicular tracks of cells resuming migration) (F) and SF3B3. A rabbit monoclonal IgG isotype control (H) was used as control. (I-J) As in F-H, TH cells were pre-stained with BODIPY TR Ceramide and RNA Select to track the polarisation of ceramide and RNA enriched structures to the synapse proximal membrane and the synaptic cleft. (I) Example of some T cell kinapses showing the release of ceramide^{+} and

RNA$^+$ vesicles in their vesicular tracks (see yellow arrows). (J) *Left:* Example of a TH synapse showing localisation of ceramide$^+$ and RNA$^+$ puncta in transit to the cSMAC. *Right*: We used the high resolution provided by TIRF structural illumination microscopy (TIRF-SIM) to visualise the arrangement of RNA$^+$ puncta. Most puncta associate to ceramide enriched ER-like structures lining the cSMAC (synaptic cleft, yellow arrows), suggesting the recruitment of RNA transport machinery to the boundary of the synaptic cleft. Scale bars = 5 µm. Imaging representative of at least three independent experiments and four different donors.

ACKNOWLEDGEMENTS

We are very grateful to our laboratory members and the Kennedy Institute of Rheumatology community for constructive scientific discussions, especially to Jonathan Webber, Štefan Balint, Alexander Mørch and Kristina Correa. We would like to thank Charity Ganskow, Lina Chen, and Heather Rada, as well as to Kellie Johnson and Ekaterina Zvezdova (both from BioLegend) for their technical support. We thank Professor Catarina E. Hioe for kindly providing the HIV-1 gp120 protein. We would also like to thank all the blood donors contributing to our study. This work was funded by Wellcome Trust Principal Research Fellowship 100262Z/12/Z, the ERC Advanced Grant (SYNECT AdG 670930), and the Kennedy Trust for Rheumatology Research (KTRR) (all three to M.L.D.). P.F.C.D was supported by EMBO Long-Term Fellowship (ALTF 1420-2015, in conjunction with the European Commission (LTFCOFUND2013, GA-2013-609409) and Marie Sklodowska-Curie Actions) and Oxford-Bristol Myers Squibb Fellowship. A.K. was supported by H2020 and the Research Council of Norway (in conjunction with Marie Sklodowska-Curie Actions 275466; to A.K.). M.F. and H.C.Y. thank the Wellcome Trust (212343/Z/18/Z) and EPSRC (EP/S004459/1). The eTIRF-SIM platform was built in collaboration with Micron

(www.micronoxford.com), an Oxford-wide advanced microscopy technology consortium supported by Wellcome Strategic Awards (091911 and 107457), and with additional funds from an MRC/EPSRC/BBSRC next-generation imaging award and the Kennedy Trust for Rheumatology Research through the Kennedy Institute Cell Dynamics Platform. Y.P., T.D. and R.F. were supported by the Chinese Academy of Medical Sciences (CAMS) Innovation Fund for Medical Sciences (CIFMS), China (grant number: 2018-I2M-2-002) and UK Medical Research Council (MRC); E.S. was supported by Newton-Katip Celebi Institutional Links grant (352333122) and SciLifeLab fellowship (to E.S.). F.S-M. was supported by grants SAF2017-82886-R from the Spanish Ministry of Economy and Competitiveness (MINECO), and "La Caixa" Banking Foundation (HR17-00016). We thank the NIH Tetramer Core Facility for the synthesis of the HLA-DRB1*09:01 monomers used in this study. We thank the Oxford Genomics Centre at the Wellcome Centre for Human Genetics (funded by Wellcome Trust grant reference 203141/Z/16/Z) for the generation and initial processing of the sequencing data. Finally, we thank the MS laboratory at the Target Discovery Institute NDM (Oxford) led by Benedikt M. Kessler. Pablo F. Céspedes is also known as Pablo F. Céspedes-Donoso (https://orcid.org/0000-0002-1641-4107).

MATERIAL AND METHODS

Ethics

Different T cell populations were isolated from leukapheresis reduction system (LRS) chambers from de-identified, non-clinical healthy donors. The non-clinical issue division of the National Health Service and the Inter-Divisional Research Ethics Committee of the University of Oxford approved the use of LRS chambers (REC 11/H0711/7 and R51997/RE001).

Isolation and expansion of human $CD4^+$, $CD8^+$ and Treg cells from peripheral blood.

Briefly, human T cells were isolated from leukoreduction system (LRS)-concentrated peripheral blood by negative immunodensity selection using either $CD4^+$, $CD8^+$ or $CD4^+CD127^{low}$ (RosetteSep™, StemCell™ Technologies, #15022, #15023, and #15361). Enriched $CD4^+$ $CD127^{low}$ cells were immediately used for fluorescence-activated cell sorting of regulatory T cells (Treg) based on low CD127 fluorescence and high CD25 fluorescence. Briefly, Tregs were sorted from enriched $CD4^+$ $CD127^{neg}$ peripheral blood cells using a FACSAria III cell sorter. A nested gating strategy was used in which $CD4^+$ $CD127^{neg}$ $CD25^{high}$ cells were gated such that only the brightest 5% of $CD25^{high}$ cells were sorted. Recovered cells were stimulated with Human T-activator CD3/CD28 Dynabeads (ThermoFisher) at a bead to cell ratio of 3:1 and 1,000 U/mL of recombinant human IL-2 (Peprotech). Fresh IL-2 containing media was added every 48 h and Human T-activator CD3/CD28 Dynabeads were added again at day 7 and removed at day 15 of expansion. This protocol allowed us the enhanced recovery of $FoxP3^+$ T cells by day 15 of expansion (see Fig. S4A-C). On the other hand, conventional $CD4^+$ and $CD8^+$ T cells were expanded using a bead to cell ratio of 1:1 and 100 U/mL of IL-2. After 3 days of activation, Human T-activator CD3/CD28 Dynabeads were removed and the conventional $CD4^+$ and $CD8^+$ cells kept in

complete RPMI media supplemented with 100 U/mL of IL-2. All BSLB synaptic transfer experiments were performed after preconditioning of T cells to IL-2-depleted complete RPMI 1640 media containing 10% of either heat-inactivated AB human serum (Treg & controls) or foetal bovine serum, and 100 µM non-essential amino acids, 10 mM HEPES, 2 mM L-glutamine, 1 mM sodium pyruvate, 100 U/ml of penicillin and 100 µg/mL of streptomycin).

Culture of CD4$^+$ T cell clones

The HLA-DRB1*09:01-restricted T cell clones 16, 35 and 40 (all specific against the influenza H3 $HA_{338-355}$ peptide: NVPEKQTRGIFGAIAGFI) were expanded using at a ratio of 1 clone: 2 feeder cells (irradiated, pooled PBMCs from 2-3 healthy donors) at a total cell concentration of 3 x 10^6 cells/mL in RPMI 1640 supplemented with 10% heat-inactivated AB human serum and 30 µg/ml of PHA for three days. Then, 100 U/ml of recombinant human IL-2 were added to fresh media, which was replaced every 2 days. Clones were used between days 8 and 12 of culture.

Production of chimeric antigen receptor (CAR) recombinant CD8$^+$ T cells

The CAR constructs that bind the NY-ESO-$1_{157-165}$ HLA-A2 pMHC complex were a kind gift from Cristoph Renner (Zurich, Switzerland) and described elsewhere [78, 79]. Briefly, the T1 CAR binds the C9V NY-ESO-1 APL with a K_D of ~2 nM. The CAR construct was packaged within third-generation self-inactivating lentiviral transfer vectors with the EF1α promoter and the Woodchuck Hepatitis Virus Post-Transcriptional Regulatory Element. The CAR features a scFv binding domain, Ig domain spacers derived from human IgG1, the CD28 transmembrane domain and the CD3ζ signalling tail. For lentiviral production, 293T cells (ATCC CRL-3216) were co-transfected with a mix of the VSV-G (370 ng), the lentiviral CAR (800 ng), and RSV-Rev and GAG (950 ng each) plasmids. The plasmid mix was

prepared in DMEM (Merck, #D6429) containing X-treme Gene HP DNA Transfection Reagent (Merck, #6366546001) and after 20 min preincubation at RT, the mix was added to 293T cells in a dropwise manner. Twenty-four h after isolation and stimulation with Human T-activator CD3/CD28 Dynabeads, $CD8^+$ T cells were transduced with freshly harvested and 0.45 µm-filtered supernatant containing 50 U/mL of recombinant human IL-2. Three days after transduction Dynabeads were removed and the cells kept in culture at a concentration of $1x10^6$ cells/mL in IL-2 supplemented RPMI media (see above). Transduction efficiency was determined between days 8-10 of culture using a polyclonal goat anti-human IgG Fc PE (ThermoFisher Scientific, #12-4998-82) and the synaptic transfer to BSLB addressed immediately.

Bead Supported Lipid Bilayers (BSLB)

Non-functionalized silica beads (5.0 µm diameter, Bangs Laboratories, Inc.) were washed extensively with PBS in 1.5 ml conical microcentrifuge tubes. BSLBs were formed by incubation with mixtures of liposomes to generate a final lipid composition of 0.2 mol% Atto-DOPE; 12.5 mol% DOGS-NTA in DOPC at a total lipid concentration of 0.4 mM. In this work, we used DOPE lipids conjugated with either Atto 390, 488, 565 or 647. The resultant BSLB were washed with 1% human serum albumin (HSA)-supplemented HEPES-buffered saline (HBS), referred herein as HBS/HSA buffer. To saturate NTA sites, BLSB were then blocked with 5% casein 100 µM $NiSO_4$ for 20 minutes. After two washes, BSLB were loaded with concentrations of His-tagged proteins required to achieve the indicated molecular densities (in range of 1-100 nM; please refer to each Figure legend). Excess proteins were removed by washing with HBS/HSA after 30 minutes. T cells (2.5×10^5/well) were incubated with BSLB at 1:1 ratio in a V-bottomed 96 well plate (Corning) for 90 min at 37ºC in 100 µl HBS/HSA. For gentle dissociation of BSLB: cell conjugates, culture plates

were gradually cooled down by incubation at RT for 15 min, followed by incubation on ice. After 45 min, cells and BSLB were centrifuged at 300 *g* for 5 min prior to resuspension in ice-cold 5% BSA in PBS pH 7.4. Single BSLB and cells were gently resuspended prior to staining for flow cytometry analysis or sorting.

Multicolour Flow Cytometry (FCM)

Staining with fluorescent dye conjugated antibodies was performed immediately after dissociation of cells and BSLB conjugates. Staining was performed in ice-cold 5% BSA in PBS pH 7.4 (0.22 µm-filtered) for a minimum of 30 min at $^{+}4^{o}$C. Then, cells and BSLB were washed three times and acquired immediately using an LSRFortessa X-20 flow cytometer equipped with a High Throughput Sampler (HTS). For absolute quantification, we used Quantum Molecules of Equivalent Soluble Fluorescent dye (MESF) beads (see below), which were first acquired to set photomultiplier voltages to position all the calibration peaks within an optimal arbitrary fluorescence units' dynamic range (between 10^1 and 2 x 10^5, and before compensation). Fluorescence spectral overlap compensation was then performed using single colour-labelled cells and BSLB, and unlabelled BSLB and cells. For markers displaying low surface expression levels unstained and single colour stained UltraComp eBeads (Thermo Fisher Scientific Inc.; #01-2222-42) were used for the calculation of compensation matrixes. After application of the resulting compensation matrix, experimental specimens and Quantum MESF beads were acquired using the same instrument settings. In most experiments acquisition was set up such as a minimum of 5 x 10^4 single BSLBs were recorded. To reduce the time of acquisition of high throughput experiments a minimum of 1 x 10^4 single BSLBs were acquired per condition instead. All dye-conjugated antibodies described in this study are listed in Table S3.

Calibration of flow cytometry (FCM) data

T cells and BSLB were analysed using antibodies with known fluorescent dye to Ab ratio (F/P) in parallel with the Quantum MESF beads (Bangs Laboratories, Inc. IN, USA), allowing the calculation of the absolute number of antibodies bound per T cell and per BSLB after subtraction of unspecific signals given by isotype control antibodies. We used MESF standard beads labelled with the Alexa Fluor® dyes 488 and 647 to estimate number of dye molecules from mean fluorescence intensities (corrected and geometric, cGMFI). Briefly, MESF beads provided 5 different populations of beads with increasing GMFI allowing the linear regression of corrected GMFI (cGMFI) over MESF. The resulting slope is then used for the interpolation of total fluorochromes bound to either BSLB or cells from cGFMI values. Since we also used antibodies with known fluorochromes per protein (F/P), we then estimated the number of bound antibodies (and hence molecules) per BSLB by dividing the estimated fluorochrome number by the detection antibody F/P value (Number of molec./event = Fluorescent molec.$_{event}$/(F/P)$_{Ab}$).

Imaging flow Cytometry (IFC)

Imaging flow Cytometry (IFC) was performed using an Amnis® ImageStream® MKII (Luminex Corporation, Austin, TX) system equipped with an 60X objective lens and 4 laser lines 488nm (100mW), 405nm (120mW), 561nm (40mW) and 642nm (150mW). Prior to sample acquisition the optical and fluidic systems were calibrated using the ASSIST protocol. Samples were acquired using 7 fluorescent channels and 2 brightfield channels. The Extended Depth of Field (EDF) mode was turned off for acquisition. Compensation matrixes were calculated for every single experiment and for further analysis. IFC data analysis was performed in IDEAS 6.2 software (Luminex Corporation, TX, USA) and FCSExpress (De Novo Software,CA, USA). The identification of singlets was performed first by Area and

Aspect Ratio Intensity, followed by the identification of BSLB and Cells based on fluorescence for DOPE Atto lipids and CD4 (Fig. S1B). Proper singlet identification was corroborated by manual curation of gated events using IDEAS software and the events exported as .tiff files. Events belonging to the BSLB gate were then centered, and stacked per channel and analysed using the Fiji EzColocalization plugin [55].

Synaptic ectosome elution from BSLB

After 90 min incubation cells and BSLBs were collected at each step of the elution process to control by FCM the release of proteins from the BSLB surface. Briefly, elution was performed as follows; first conjugates were cooled down 15 min at RT and then 40 min on ice to gentle separate cells and BSLB. Then, conjugate suspensions were centrifuged at 100*g* for 1 min and $^{+}4^{o}$C to enrich for BSLB. After two washes with ice cold PBS pH 7.4, BSLB were resuspended in ice-cold 50 mM EDTA in PBS pH 7.4 for 2h. BSLB-free supernatants were then centrifuged at $^{+}4^{o}$C in sequential steps at 300*g* for 5 min (twice), then at 2,000*g* for 10 min and 10,000*g* for 10 min. Finally, recovered supernatants were centrifuged at 120,000*g* for 4h at $^{+}4^{o}$C and the pellets washed once more with PBS pH 7.4 and kept at $^{+}4^{o}$C or frozen at -80 ^{o}C until analyses by either NTA, NanoFCM or immunoblotting. T cell sEVs were isolated by the same differential centrifugation procedure indicated above. To minimize serum contamination, T cells were cultured in OptiMEM-I supplemented with 100 U/mL of IL-2 for sEV purification.

Nanoparticle Tracking Analysis

Eluted SV and sEV preparations were resuspended in PBS in a 1:100 dilution and kept on ice for Nanoparticle Tracking Analysis (NTA). The instrument used for NTA was Nanosight NS300 (Malvern Instruments Ltd) set on light scattering mode and instrument sensitivity of

15. Measurements were taken with the aid of a syringe pump to improve reproducibility. Three sequential recordings of 60 seconds each were obtained per sample and NTA 3.2 software was used to process and average the three recordings to determine the mean size.

Nano Flow Cytometry

Flow NanoAnalyzer model type N30E (NanoFCM Inc., Xiamen, China) that allows single ex osomes detection was used to determine the size distribution and granular concentration of E Vs. The Nano-flow cytometry analysis was performed using the Flow NanoAnalyzer (NanoFCM Co., LTD) according to manufacturer's instructions. The Silica Nanospheres Cocktail (S16M-Exo, NanoFCM) was employed as the size standard to construct a calibration curve to allow the conversion of side scatter intensities to particle size. A concentration standard (200nm PS QC beads, NanoFCM) was used to measure particle concentration. The laser used was a 488nm laser at 25/40 mW, 10% ss decay. Lens filters equipped were 525/40 (AF488) and 580/40 (PE).

Planar Supported Lipid Bilayers (PSLB)

Liposome mixtures were injected into flow chambers formed by sealing acid piranha and plasma-cleaned glass coverslips to adhesive backed plastic manifolds with 6 flow channels (StickySlide VI 0.4; Ibidi). After 30 minutes the channels were flushed with HBS-HSA without introducing air bubbles to remove excess Liposomes. After blocking for 20 min with 5% casein supplemented with 100 µM $NiCl_2$, to saturate NTA sites, followed by washing and then His-tagged proteins were incubated on bilayers for additional 30 min. Protein concentrations required to achieve desired densities on bilayers were calculated from calibration curves constructed from FCM measurements on BSLB and analysed alongside MESF beads (MESF; Quantum™ Bangs Laboratories Inc.). Bilayers were continuous liquid

disordered phase as determined by fluorescence recovery after photobleaching with a 10 µm bleach spot on an FV1200 confocal microscope (Olympus).

Immunological Synapse formation on PSLB

Prior to immunological synapse imaging, primary T cell blasts were washed twice and resuspended in prewarmed HBS/HSA buffer to a final concentration of 5 x 10^6 cells/mL. Then, 5 x 10^5 T cells were stimulated for 20 min at 37°C and 5% CO_2 over PSLB containing 30 molec./µm^2 anti-CD3ε Fab (clone UCHT-1; Alexa Fluor® (AF) 488 or unlabelled), 200 molec./µm^2 of ICAM1 AF405, and 100 molec./µm^2 of CD40 (AF488 or unlabelled). Then, cells were stained with 1 µg/mL of wheat germ agglutinin (WGA) conjugated to CF568 (Biotium; #29077-1) and 1 µg/mL anti-CD154 (CD40L) clone 24-31 AF647 for 15 min at RT and in the dark. Cells were washed three times with 5% BSA 20 mM HEPES 2 mM $MgCl_2$ in PBS and fixed with pre-warmed 4% electron microscopy grade formaldehyde in PHEM buffer (10 mM EGTA, 2 mM $MgCl_2$, 60 mM Pipes, 25 mM HEPES, pH 7.0) for 20 min at RT and in the dark. After two washes, cells were kept in HBS/HSA until imaging by TIRFM. For intracellular staining, cells were permeabilized for 3 min with 0.1% Triton X-100 in PBS, washed and blocked for 60 min with 5% BSA in PBS before staining with primary antibodies (1 µg/mL for 1h at RT). Primary antibodies included Rabbit anti-human TSG101 clone EPR7130B AF647 (#ab207664), anti-human YB1 (YBX1) clone EPR22682-2 (#ab255606), anti-human SF3B3 clone EPR18440 (#ab209402), and Rabbit Isotype control EPR25A AF647 (#ab199093). After three washes, cells were blocked with 0.22 µm-filtered 5% Donkey Serum for 1 h at RT before staining for 1h with AF647 AffiniPure F(ab')□ Fragment Donkey Anti-Rabbit IgG (H+L) (Jackson ImmunoResearch, #711-606-152). After four washes, cells were washed and then stained with anti-Vimentin clone EPR3776 AF555 (#ab203428). Cells were washed four times before acquisition.

TIRFM

TIRFM was performed on an Olympus IX83 inverted microscope equipped with a 4-line (405 nm, 488 nm, 561 nm, and 640 nm laser) illumination system. The system was fitted with an Olympus UApON 150x 1.45 numerical aperture objective, and a Photometrics Evolve delta EMCCD camera to provide Nyquist sampling. Quantification of fluorescence intensity was performed with Fiji/ImageJ (National Institute of Health) and MATLAB R2019b. A batch measure macro was used to automatically segment cell:SLB contacts based on internal reflection microscopy followed by both background subtraction and the measure of fluorescence across different channels.

TIRF-SIM

A custom-built eTIRF-SIM microscope system was used and detailed elsewhere[80]. Structured illumination was obtained via a grating pattern generated by a ferroelectric spatial light modulator (SLM, Forth Dimension Displays, QXGA3DM). After, the first diffraction orders are selected by the mask and sent to the Olympus IX83 microscope head. The distance between diffraction orders were tuned by SLM settings ultimately defining the illumination angle and therefore the TIRF depth. Excitation wavelengths of 488 nm, 560 nm, and 640 nm were used (MPB communications Inc., 500mW, 2RU-VFL-P-500-488-B1R, 2RU-VFL-P-500-560-B1R). Sample illumination was carried out using a high-NA TIRF objective (Olympus Plan-Apochromat 100X 1.49NA). The emitted fluorescence was collected by the same objective and sent onto sCMOS cameras recording the raw data (Hamamatsu, Orca Flash 4.0 v2 sCMOS). The excitation numerical aperture (NA) was adjusted for each wavelength by changing the period of the grating pattern at the SLM, which allows controlling the TIRF angle and, therefore, the penetration depth of the evanescent wave. To

achieve TIRF-SIM illumination at the interface between the cells and SLB, both excitation lights were sent with an incident NA ranging from 1.38 to 1.41. Prior to experiment acquisition alignment was perform by imaging 100 nm Tetraspeck fluorescent beads in all three excitation colours. Then, using Fiji plugin MultiStackReg – the beads images were used to adjust images and compensate for chromatic aberrations. A total of 9 raw images were acquired per frame and for a single excitation wavelength before switching to the next wavelength. Then, raw images were processed and reconstructed into SIM images by custom made software or ImageJ fairSIM plugin. All experiments were performed at physiological conditions using a micro-incubator (H301, Okolabs, Italy) at 37 °C and 5% CO_2. For each frame, we used an acquisition time between 20 and 300 ms depending on the fluorescence signal levels and 2 colours, 18 frames total) every 0.4–5 s. One colour super-resolved image was reconstructed from 9 raw image frames (3 angles and 3 phases) using a reconstruction method described previously [81, 82].

CRISPR/Cas9 genome editing

After 48 h of stimulation with Human T-activator CD3/CD28 Dynabeads (ThermoFisher) $CD4^+$ lymphoblasts were recovered for transfection of CRISPR/Cas9 nucleoprotein complexes. Briefly, tracer RNA and crRNAs were mixed at equimolar concentrations (200 µM) and incubated at 95^{o}C for 15 min. After cooling the gRNA mix down to RT, the Cas9 enzyme was added at final 20 µM (IDT, #1081061). After 15 min incubation at 37^{o}C, electroporation enhancer was added to CRISPR-Cas9 nucleoprotein complexes following manufacturer's guidelines, and immediately mixed with 1.5 x 10^6 cells. Cells were then transferred to a 2-mm cuvette (Bio-Rad) and electroporated at 300V for 2ms using an ECM830 Square Wave electroporator (BTX). Immediately after transfection, cells were recovered with pre-warmed, IL-2 supplemented RPMI 1640 media and expanded for another

6 days. Synaptic transfer experiments to BSLB or planar SLB were performed on day 7 or 8 of culture and protein expression controls were carried out in parallel. All crRNAs sequences are summarised in Table S5 (all on- and off-target scores were optimised by the crRNA supplier (IDT)).

Western Blotting

Whole cell lysates (WCL) were prepared by resuspending cell pellets in RIPA lysis and extraction buffer (Thermo Fisher Scientific, #89901) containing a Protease/Phosphatase inhibitor cocktail (Cell Signaling Technology (CST); #5872) to a final concentration of 2 x 10^7 cells/mL. After sonication at +4^{o}C (10 cycles of 30 s on/30 s off), WCL were centrifuged at 10,000*g* for 10 min at $^+$4^{o}C, and the supernatants collected, mixed with loading solution and denatured at $^+$95^{o}C for 10 min. For immunoblotting of BSLB eluted material, after centrifugation at 120,000*g* for 4 h at $^+$4^{o}C, pellets were resuspended in RIPA lysis buffer containing a Protease/Phosphatase inhibitor cocktail, mixed with loading solution and denatured at $^+$95^{o}C for 10 min. When indicated, lysed eluates from 3 x 10^7 BSLB were loaded with either only ICAM-1 (control) or ICAM-1 + anti-CD3ε-Fab were used per lane. As positive control for CD40L detection WCL equivalent to 2.25 x 10^5 CD4$^+$ lymphoblasts was used per lane. Similarly, for CRISPR/Cas9 edited cells, WCL equivalent to 3 x 10^5 cells were used per lane. Samples were resolved using 4-15% Mini-PROTEAN SDS-PAGE gel (Bio-Rad; #4561084), transferred to 0.45 µm nitrocellulose membranes (Bio-Rad, #1620115), blocked and incubated with the following primary antibodies: rabbit anti-human CD40 Ligand clone D5J9Y (CST, #15094), rabbit anti-GAPDH clone D16H11 (CST, #5174), mouse anti-β-actin clone 8H10D10 (CST, #3700), and rabbit anti-TSG101 clone EPR7130B (#ab125011). Then, membranes were incubated with IRDye® 680RD donkey anti-mouse IgG (H+L; LI-COR, #926-68072) and IRDye® 800CW donkey anti-rabbit IgG

(H+L; LI-COR, #925-32213) secondary antibodies following manufacturer guidelines. After four washes, membranes were imaged and analysed using the Odyssey® CLx Near-Infrared detection system equipped with the Image Studio™ Lite quantification software (LI-COR, Lincoln, NE).

RNA sequencing and miR analyses

Total cell RNA was extracted using the miRNeasy Tissue/Cells Advanced Mini Kit (Qiagen, #217604). Purified RNA yields and quality were assessed via Agilent 2100 Bioanalyzer using the Agilent 6000 RNA Pico chips (Agilent Technologies, # 5067-1513). Before library preparation the material was further quantified using RiboGreen (Invitrogen) on the FLUOstar OPTIMA plate reader (BMG Labtech) and the size profile and integrity analysed on the 2200 or 4200 TapeStation (Agilent, RNA ScreenTape). Input material was normalised to 200 ng or maximum mass for input volume prior to library preparation. Small RNA library preparation was completed using NEBNext Small RNA kit (NEB) following manufacturer's instructions and applying the low input protocol modifications. Libraries were amplified (15 cycles) on a Tetrad (Bio-Rad) using in-house unique dual indexing primers as described elsewhere [83]. Size selection was performed using Pippin Prep instrument (Sage Science) using the 3% Agarose, dye free gel with internal standards (size selection: 120 to 230bp). Individual libraries were normalised using Qubit, and the size profile was analysed on the 2200 or 4200 TapeStation. 10 nM libraries were denatured and further diluted prior to loading on the sequencer. Two runs of single end sequencing were performed; run one was performed in an Illumina HiSeq 2500 system (1x60) and run two was performed using Illumina NextSeq 500/550 v2.5 Kits (75 cycles). Quality control and processing of the raw sequencing data was performed using sRNAbench [84] and miRQC [85] which allowed the assessment of sequencing yield, quality, percentage of miR-mapping reads, read length

distribution and relative abundance of fragments from other RNA species. Functional and biological pathway enrichment analyses were performed on annotated miR species shared between the two independent sequencing runs and enriched in each EV category (i.e., SV and sEV). MIENTURNET and the KEGG annotation database were used. Statistical analysis for functional and biological pathway enrichment analyses using MIENTURNET were carried out by calculating the *P*-value resulting from the hypergeometric test. Motif analyses of bulk, enriched miR sequences in each sample were performed using MEME (Multiple Em for Motif Elucidation 5.1.0) [40]. To dissect the miR-target gene interactome of our enriched miR we used miRNet 2.0 [86] by first mapping input miR to the miR interaction knowledgebase comprising annotations from miRbase, miTarBase and ExoCarta together with interactions with other miR, genes and transcription factors from TransmiR 2.0, ENCODE, JASPAR and ChEA. The output of the 'miRs' module of miRNet 2.0 provided the motif miR-target gene interactome enrichment analysis. We used FunSet [87] to graphically plot gene ontology (GO) enrichment analyses in 2D plots clustering GO terms based on semantic similarities and extracting representative terms for each cluster. The result of GO enrichment analysis using Funset was filtered by setting the FDR threshold to 0.05 (using the Benjamini-Hochberg procedure) and the *P*-values were calculated using the hypergeometric test.

Mass spectrometry

Samples isolated by differential centrifugation were concentrated using 100,000 NMWL centrifugal filters (Amicon® Ultra, #UFC510024, Merck Millipore Ltd.) and prepared in S-Trap™ spin columns (#C02-micro-80) following manufacturer recommendations. Briefly, samples were reduced with 5 µL of 10 mM TCEP and alkylated with 50 mM of IAA for 30 min each, then acidified with 12% phosphoric acid 10:1 vol:vol, and then transferred to S-

trap columns. Then, samples were precipitated using 1:8 vol:vol dilution of each sample in 90% methanol in 100 mM TEAB. Samples were then washed three times with 90% methanol in 100 mM TEAB. Samples were then resuspended in 50 µL of 50 mM TEAB and digested with trypsin (Promega, #V1115) overnight at 37^{o}C. Peptides were eluted from the S-Trap by spinning for 1 min at 1,500*g* with 80 µL of 50 mM ammonium bicarbonate, 80 µL 0.1% FA and finally 80 mL of 50% ACN 0.1% FA. The eluates were dried down in a vacuum centrifuge and resuspended in 2% ACN 0.1% TFA prior to off-line high-pH reversed-phase fractionation using RP-S cartridges pre-primed with 100 µL ACN at 300 µL/min and equilibrated with 50 µL of 2% ACN 0.1% TFA at 10 µL/min. Samples were loaded at 5 mL/min and divided into 8 fractions (elution steps), which were run individually. Elutions were performed with increasing concentrations of 90% ACN, pH 10 in water, including final 5%, 10%, 12.5%, 15%, 20%, 22.5%, 25% and 50%. Fractions were further dried down in a vacuum centrifuge and resuspended in loading buffer. For LC-MS/MS acquisition 50-80 ng peptides were loaded onto preconditioned Evotips containing 0.1% FA in water. Preconditioning was performed by pre-priming of isopropanol-soaked tips with 20 µL of ACN 0.1% FA, following by centrifugation for 1 min at 700*g*, equilibration in water 0.1% FA and a final centrifugation for 1 min at 700*g*). Samples were run on a LC-MS system comprised of an Evosep One and Bruker timsTOF Pro. Peptides were separated on an 8 cm analytical C18 column (Evosep, 3 µm beads, 100 µm ID) using the pre-set 60 samples per day gradient on the Evosep One. Acquisition was done in PASEF mode (4 PASEF frames, 3 cycles overlap, oTOF control v6.0.0.12) including an ion mobility window between 1/k0 start=0.85 Vs/cm2 to 1/k0 end = 1.3 Vs/cm^2, a ramp time of 100 ms with locked duty cycle and a mass range of 100-1,700 m/z. For proteomic analyses the raw files were searched against the reviewed Uniprot *Homo sapiens* database (retrieved 2,01,80,131) using

MaxQuant version 1.6.10.43 [88] and its built-in contaminant database using tryptic specificity and allowing two missed cleavages.

Statistical Analyses

Normality tests were performed using either Shapiro-Wilk or Kolmogorov-Smirnov tests. Statistical significance was determined by multiple comparisons performed either by one-way analysis of variance (ANOVA) or Kruskal-Wallis (corrected by Holm-Sidak or Dunn's, respectively). Non-linear regressions using three or four parameters F-tests were also performed when indicated. All statistical tests were performed in GraphPad Prism v8 and are detailed in each figure legend. Means of significance are as follows: *$p < 0.05$, ** $p < 0.005$, ***$p < 0.0005$, and ****$p < 0.0001$.

REFERENCES

1. Choudhuri, K., et al., *Polarized release of T-cell-receptor-enriched microvesicles at the immunological synapse.* Nature, 2014. **507**(7490): p. 118-23.
2. Saliba, D.G., et al., *Composition and structure of synaptic ectosomes exporting antigen receptor linked to functional CD40 ligand from helper T cells.* Elife, 2019. **8**.
3. Balint, S., et al., *Supramolecular attack particles are autonomous killing entities released from cytotoxic T cells.* Science, 2020. **368**(6493): p. 897-901.
4. Cespedes, P.F., et al., *Model membrane systems to reconstitute immune cell signaling.* FEBS J, 2020.
5. Vasiliver-Shamis, G., et al., *Human immunodeficiency virus type 1 envelope gp120 induces a stop signal and virological synapse formation in noninfected CD4+ T cells*. J Virol, 2008. **82**(19): p. 9445-57.
6. Vasiliver-Shamis, G., et al., *Human immunodeficiency virus type 1 envelope gp120-induced partial T-cell receptor signaling creates an F-actin-depleted zone in the virological synapse.* J Virol, 2009. **83**(21): p. 11341-55.
7. Mittelbrunn, M., et al., *Unidirectional transfer of microRNA-loaded exosomes from T cells to antigen-presenting cells.* Nat Commun, 2011. **2**: p. 282.
8. Fernandez-Messina, L., et al., *Transfer of extracellular vesicle-microRNA controls germinal center reaction and antibody production.* EMBO Rep, 2020. **21**(4): p. e48925.
9. Torralba, D., et al., *Priming of dendritic cells by DNA-containing extracellular vesicles from activated T cells through antigen-driven contacts.* Nat Commun, 2018. **9**(1): p. 2658.
10. Liu, J., et al., *Archaeal extracellular vesicles are produced in an ESCRT-dependent manner and promote gene transfer and nutrient cycling in extreme environments.* ISME J, 2021.
11. Chouaki-Benmansour, N., et al., *Phosphoinositides regulate the TCR/CD3 complex membrane dynamics and activation.* Sci Rep, 2018. **8**(1): p. 4966.
12. Schneider, F., et al., *Diffusion of lipids and GPI-anchored proteins in actin-free plasma membrane vesicles measured by STED-FCS.* Mol Biol Cell, 2017. **28**(11): p. 1507-1518.
13. Beckers, D., D. Urbancic, and E. Sezgin, *Impact of Nanoscale Hindrances on the Relationship Between Lipid Packing and Diffusion in Model Membranes.* J Phys Chem B, 2020.
14. Han, J., et al., *Role of substrates and products of PI 3-kinase in regulating activation of Rac-related guanosine triphosphatases by Vav*. Science, 1998. **279**(5350): p. 558-60.
15. Bilanges, B., Y. Posor, and B. Vanhaesebroeck, *PI3K isoforms in cell signalling and vesicle trafficking.* Nat Rev Mol Cell Biol, 2019. **20**(9): p. 515-534.
16. Wang, T., et al., *Dynasore-induced potent ubiquitylation of the exon 19 deletion mutant of epidermal growth factor receptor suppresses cell growth and migration in non-small cell lung cancer.* Int J Biochem Cell Biol, 2018. **105**: p. 1-12.
17. Isaaz, S., et al., *Serial killing by cytotoxic T lymphocytes: T cell receptor triggers degranulation, re-filling of the lytic granules and secretion of lytic proteins via a non-granule pathway.* Eur J Immunol, 1995. **25**(4): p. 1071-9.
18. Li, J.H., et al., *The regulation of CD95 ligand expression and function in CTL.* J Immunol, 1998. **161**(8): p. 3943-9.

19. Hong, J., et al., *Lysosomal regulation of extracellular vesicle excretion during d-ribose-induced NLRP3 inflammasome activation in podocytes.* Biochim Biophys Acta Mol Cell Res, 2019. **1866**(5): p. 849-860.
20. Melikova, M.S., K.A. Kondratov, and E.S. Kornilova, *Two different stages of epidermal growth factor (EGF) receptor endocytosis are sensitive to free ubiquitin depletion produced by proteasome inhibitor MG132.* Cell Biol Int, 2006. **30**(1): p. 31-43.
21. Sundquist, W.I., et al., *Ubiquitin recognition by the human TSG101 protein.* Mol Cell, 2004. **13**(6): p. 783-9.
22. Milhas, D., et al., *Anterograde and retrograde transport of neutral sphingomyelinase-2 between the Golgi and the plasma membrane.* Biochim Biophys Acta, 2010. **1801**(12): p. 1361-74.
23. Tomiuk, S., M. Zumbansen, and W. Stoffel, *Characterization and subcellular localization of murine and human magnesium-dependent neutral sphingomyelinase.* J Biol Chem, 2000. **275**(8): p. 5710-7.
24. Borger, J.G., R. Zamoyska, and D.M. Gakamsky, *Proximity of TCR and its CD8 coreceptor controls sensitivity of T cells.* Immunol Lett, 2014. **157**(1-2): p. 16-22.
25. Yokosuka, T., et al., *Spatiotemporal regulation of T cell costimulation by TCR-CD28 microclusters and protein kinase C theta translocation.* Immunity, 2008. **29**(4): p. 589-601.
26. Munoz, P., et al., *Antigen-induced clustering of surface CD38 and recruitment of intracellular CD38 to the immunologic synapse*. Blood, 2008. **111**(7): p. 3653-64.
27. Cockayne, D.A., et al., *Mice deficient for the ecto-nicotinamide adenine dinucleotide glycohydrolase CD38 exhibit altered humoral immune responses.* Blood, 1998. **92**(4): p. 1324-33.
28. Han, L., et al., *Phenotypical analysis of ectoenzymes CD39/CD73 and adenosine receptor 2A in CD4(+) CD25(high) Foxp3(+) regulatory T-cells in psoriasis.* Australas J Dermatol, 2018. **59**(1): p. e31-e38.
29. Samudra, A.N., et al., *CD39 and CD73 activity are protective in a mouse model of antiphospholipid antibody-induced miscarriages.* J Autoimmun, 2018. **88**: p. 131-138.
30. Allard, B., et al., *The ectonucleotidases CD39 and CD73: Novel checkpoint inhibitor targets*. Immunol Rev, 2017. **276**(1): p. 121-144.
31. Clayton, A., et al., *Cancer exosomes express CD39 and CD73, which suppress T cells through adenosine production.* J Immunol, 2011. **187**(2): p. 676-83.
32. Lang, I., et al., *Binding Studies of TNF Receptor Superfamily (TNFRSF) Receptors on Intact Cells.* J Biol Chem, 2016. **291**(10): p. 5022-37.
33. Schubert, D.A., et al., *Self-reactive human CD4 T cell clones form unusual immunological synapses.* J Exp Med, 2012. **209**(2): p. 335-52.
34. Demetriou, P., et al., *A dynamic CD2-rich compartment at the outer edge of the immunological synapse boosts and integrates signals.* Nat Immunol, 2020. **21**(10): p. 1232-1243.
35. Ivey-Hoyle, M., et al., *Envelope glycoproteins from biologically diverse isolates of immunodeficiency viruses have widely different affinities for CD4.* Proc Natl Acad Sci U S A, 1991. **88**(2): p. 512-6.
36. Deng, J., et al., *HIV Envelope gp120 Alters T Cell Receptor Mobilization in the Immunological Synapse of Uninfected CD4 T Cells and Augments T Cell Activation.* J Virol, 2016. **90**(23): p. 10513-10526.
37. Schulte, M., et al., *ADAM10 regulates FasL cell surface expression and modulates FasL-induced cytotoxicity and activation-induced cell death*. Cell Death Differ, 2007. **14**(5): p. 1040-9.

38. Ebsen, H., et al., *Subcellular localization and activation of ADAM proteases in the context of FasL shedding in T lymphocytes*. Mol Immunol, 2015. **65**(2): p. 416-28.
39. Yacoub, D., et al., *CD154 is released from T-cells by a disintegrin and metalloproteinase domain-containing protein 10 (ADAM10) and ADAM17 in a CD40 protein-dependent manner*. J Biol Chem, 2013. **288**(50): p. 36083-93.
40. Bailey, T.L., et al., *MEME SUITE: tools for motif discovery and searching*. Nucleic Acids Res, 2009. **37**(Web Server issue): p. W202-8.
41. Dooley, K., et al., *A versatile platform for generating engineered extracellular vesicles with defined therapeutic properties.* Mol Ther, 2021. **29**(5): p. 1729-1743.
42. Shurtleff, M.J., et al., *Y-box protein 1 is required to sort microRNAs into exosomes in cells and in a cell-free reaction.* Elife, 2016. **5**.
43. Shurtleff, M.J., et al., *Broad role for YBX1 in defining the small noncoding RNA composition of exosomes.* Proc Natl Acad Sci U S A, 2017. **114**(43): p. E8987-E8995.
44. Bruno Vaz, C.V., Salvatore Valvo, Clara D'Ambra, Francesco Maria Esposito, Valerio Chiurchiù, Oliver Devine, Massimo Sanchez, Giovanna Borsellino, Derek Gilroy, Arne N. Akbar, Michael L. Dustin, Michael Karin, Alessio Lanna, *Intercellular telomere transfer extends T cell lifespan.* bioRxiv, 2020.
45. Gay, D., et al., *The major histocompatibility complex-restricted antigen receptor on T cells. IX. Role of accessory molecules in recognition of antigen plus isolated IA.* J Immunol, 1986. **136**(6): p. 2026-32.
46. Biswas, K.H. and J.T. Groves, *A Microbead Supported Membrane-Based Fluorescence Imaging Assay Reveals Intermembrane Receptor-Ligand Complex Dimension with Nanometer Precision.* Langmuir, 2016. **32**(26): p. 6775-80.
47. Gagnon, E., et al., *Local changes in lipid environment of TCR microclusters regulate membrane binding by the CD3epsilon cytoplasmic domain.* J Exp Med, 2012. **209**(13): p. 2423-39.
48. Kim, H.R., et al., *T cell microvilli constitute immunological synaptosomes that carry messages to antigen-presenting cells.* Nat Commun, 2018. **9**(1): p. 3630.
49. Ghosh, S., et al., *ERM-Dependent Assembly of T Cell Receptor Signaling and Co-stimulatory Molecules on Microvilli prior to Activation.* Cell Rep, 2020. **30**(10): p. 3434-3447 e6.
50. Dong, R., et al., *Rewired signaling network in T cells expressing the chimeric antigen receptor (CAR).* EMBO J, 2020: p. e104730.
51. Chevillet, J.R., et al., *Quantitative and stoichiometric analysis of the microRNA content of exosomes.* Proc Natl Acad Sci U S A, 2014. **111**(41): p. 14888-93.
52. Flynn, R.A., et al., *Small RNAs are modified with N-glycans and displayed on the surface of living cells.* Cell, 2021.
53. Manuel Albanese, A.Y.-F.C., Corinna Hüls, Kathrin Gärtner, Takanobu Tagawa, Oliver T. Keppler, Christine Göbel, Reinhard Zeidler, Wolfgang Hammerschmidt, *Micro RNAs are minor constituents of extracellular vesicles and are hardly delivered to target cells.* bioRxiv, 2020.
54. Kowal, J., et al., *Proteomic comparison defines novel markers to characterize heterogeneous populations of extracellular vesicle subtypes.* Proc Natl Acad Sci U S A, 2016. **113**(8): p. E968-77.
55. Stauffer, W., H. Sheng, and H.N. Lim, *EzColocalization: An ImageJ plugin for visualizing and measuring colocalization in cells and organisms.* Sci Rep, 2018. **8**(1): p. 15764.
56. Macia, E., et al., *Dynasore, a cell-permeable inhibitor of dynamin.* Dev Cell, 2006. **10**(6): p. 839-50.

57. Uchida, R., et al., *Alutenusin, a specific neutral sphingomyelinase inhibitor, produced by Penicillium sp. FO-7436.* J Antibiot (Tokyo), 1999. **52**(6): p. 572-4.
58. Bowman, E.J., A. Siebers, and K. Altendorf, *Bafilomycins: a class of inhibitors of membrane ATPases from microorganisms, animal cells, and plant cells.* Proc Natl Acad Sci U S A, 1988. **85**(21): p. 7972-6.
59. Brown, S.S. and J.A. Spudich, *Cytochalasin inhibits the rate of elongation of actin filament fragments.* J Cell Biol, 1979. **83**(3): p. 657-62.
60. Bubb, M.R., et al., *Effects of jasplakinolide on the kinetics of actin polymerization. An explanation for certain in vivo observations.* J Biol Chem, 2000. **275**(7): p. 5163-70.
61. Campi, G., R. Varma, and M.L. Dustin, *Actin and agonist MHC-peptide complex-dependent T cell receptor microclusters as scaffolds for signaling.* J Exp Med, 2005. **202**(8): p. 1031-6.
62. Chege, N.W. and S.R. Pfeffer, *Compartmentation of the Golgi complex: brefeldin-A distinguishes trans-Golgi cisternae from the trans-Golgi network.* J Cell Biol, 1990. **111**(3): p. 893-9.
63. Helms, J.B. and J.E. Rothman, *Inhibition by brefeldin A of a Golgi membrane enzyme that catalyses exchange of guanine nucleotide bound to ARF.* Nature, 1992. **360**(6402): p. 352-4.
64. Kucik, D.F., et al., *Adhesion-activating phorbol ester increases the mobility of leukocyte integrin LFA-1 in cultured lymphocytes.* J Clin Invest, 1996. **97**(9): p. 2139-44.
65. Kupfer, A. and G. Dennert, *Reorientation of the microtubule-organizing center and the Golgi apparatus in cloned cytotoxic lymphocytes triggered by binding to lysable target cells.* J Immunol, 1984. **133**(5): p. 2762-6.
66. Lyubchenko, T.A., G.A. Wurth, and A. Zweifach, *The actin cytoskeleton and cytotoxic T lymphocytes: evidence for multiple roles that could affect granule exocytosis-dependent target cell killing.* J Physiol, 2003. **547**(Pt 3): p. 835-47.
67. Shaikh, S., et al., *Bafilomycin-A1 and ML9 Exert Different Lysosomal Actions to Induce Cell Death.* Curr Mol Pharmacol, 2019. **12**(4): p. 261-271.
68. Teplova, V.V., et al., *Bafilomycin A1 is a potassium ionophore that impairs mitochondrial functions.* J Bioenerg Biomembr, 2007. **39**(4): p. 321-9.
69. Tsai, C.C., et al., *Dynasore inhibits rapid endocytosis in bovine chromaffin cells.* Am J Physiol Cell Physiol, 2009. **297**(2): p. C397-406.
70. Tskvitaria-Fuller, I., et al., *Regulation of sustained actin dynamics by the TCR and costimulation as a mechanism of receptor localization.* J Immunol, 2003. **171**(5): p. 2287-95.
71. Young, W.W., Jr., M.L. Allende, and E. Jaskiewicz, *Reevaluating the effect of Brefeldin A (BFA) on ganglioside synthesis: the location of GM2 synthase cannot be deduced from the inhibition of GM2 synthesis by BFA.* Glycobiology, 1999. **9**(7): p. 689-95.
72. Datta, A., et al., *Manumycin A suppresses exosome biogenesis and secretion via targeted inhibition of Ras/Raf/ERK1/2 signaling and hnRNP H1 in castration-resistant prostate cancer cells.* Cancer Lett, 2017. **408**: p. 73-81.
73. Tuladhar, A. and K.S. Rein, *Manumycin A Is a Potent Inhibitor of Mammalian Thioredoxin Reductase-1 (TrxR-1).* ACS Med Chem Lett, 2018. **9**(4): p. 318-322.
74. Pasquier, B., *SAR405, a PIK3C3/Vps34 inhibitor that prevents autophagy and synergizes with MTOR inhibition in tumor cells.* Autophagy, 2015. **11**(4): p. 725-6.
75. Ronan, B., et al., *A highly potent and selective Vps34 inhibitor alters vesicle trafficking and autophagy.* Nat Chem Biol, 2014. **10**(12): p. 1013-9.

76. Pardo, J., et al., *Differential implication of protein kinase C isoforms in cytotoxic T lymphocyte degranulation and TCR-induced Fas ligand expression.* Int Immunol, 2003. **15**(12): p. 1441-50.
77. Mi, H., et al., *PANTHER version 16: a revised family classification, tree-based classification tool, enhancer regions and extensive API.* Nucleic Acids Res, 2021. **49**(D1): p. D394-D403.
78. Jakka, G., et al., *Antigen-specific in vitro expansion of functional redirected NY-ESO-1-specific human CD8+ T-cells in a cell-free system.* Anticancer Res, 2013. **33**(10): p. 4189-201.
79. Maus, M.V., et al., *An MHC-restricted antibody-based chimeric antigen receptor requires TCR-like affinity to maintain antigen specificity*. Mol Ther Oncolytics, 2016. **3**: p. 1-9.
80. Li, D., et al., *ADVANCED IMAGING. Extended-resolution structured illumination imaging of endocytic and cytoskeletal dynamics.* Science, 2015. **349**(6251): p. aab3500.
81. Barbieri, L., et al., *Two-dimensional TIRF-SIM-traction force microscopy (2D TIRF-SIM-TFM).* Nat Commun, 2021. **12**(1): p. 2169.
82. Li, D., et al., *Astigmatic traction force microscopy (aTFM).* Nat Commun, 2021. **12**(1): p. 2168.
83. Lamble, S., et al., *Improved workflows for high throughput library preparation using the transposome-based Nextera system.* BMC Biotechnol, 2013. **13**: p. 104.
84. Aparicio-Puerta, E., et al., *sRNAbench and sRNAtoolbox 2019: intuitive fast small RNA profiling and differential expression.* Nucleic Acids Res, 2019. **47**(W1): p. W530-W535.
85. Aparicio-Puerta, E., et al., *mirnaQC: a webserver for comparative quality control of miRNA-seq data.* Nucleic Acids Res, 2020. **48**(W1): p. W262-W267.
86. Chang, L., et al., *miRNet 2.0: network-based visual analytics for miRNA functional analysis and systems biology*. Nucleic Acids Res, 2020. **48**(W1): p. W244-W251.
87. Hale, M.L., I. Thapa, and D. Ghersi, *FunSet: an open-source software and web server for performing and displaying Gene Ontology enrichment analysis.* BMC Bioinformatics, 2019. **20**(1): p. 359.
88. Cox, J., et al., *Andromeda: a peptide search engine integrated into the MaxQuant environment*. J Proteome Res, 2011. **10**(4): p. 1794-805.

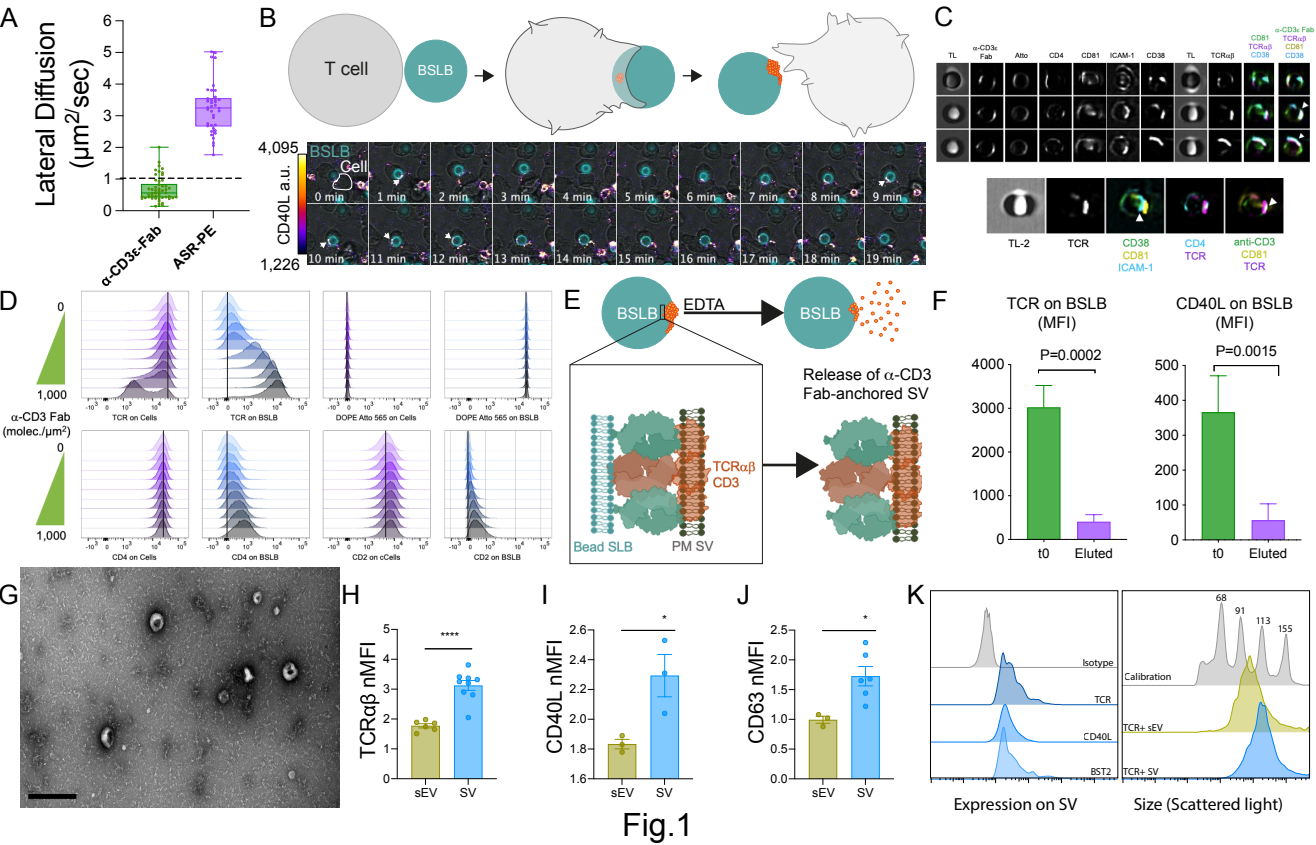
A
Lateral Diffusion (μm²/sec)
α-CD3ε-Fab
ASR-PE
B
T cell
BSLB
CD40L a.u.
4,095
1,226
BSLB
Cell
0 min
1 min
2 min
3 min
4 min
5 min
6 min
7 min
8 min
9 min
10 min
11 min
12 min
13 min
14 min
15 min
16 min
17 min
18 min
19 min
C
TL
α-CD3ε Fab
Atto
CD4
CD81
ICAM-1
CD38
TL
TCRαβ
α-CD3ε Fab
CD81
TCRαβ
CD81
CD38
TL-2
TCR
CD38
CD81
ICAM-1
CD4
TCR
anti-CD3
CD81
TCR
D
0
1,000
α-CD3 Fab (molec./μm²)
TCR on Cells
TCR on BSLB
DOPE Atto 565 on Cells
DOPE Atto 565 on BSLB
CD4 on Cells
CD4 on BSLB
CD2 on cCells
CD2 on BSLB
E
BSLB
EDTA
BSLB
Release of α-CD3 Fab-anchored SV
TCRαβ
CD3
Bead SLB
PM SV
F
TCR on BSLB (MFI)
P=0.0002
CD40L on BSLB (MFI)
P=0.0015
t0
Eluted
t0
Eluted
G
H
TCRαβ nMFI
****
sEV
SV
I
CD40L nMFI
*
sEV
SV
J
CD63 nMFI
*
sEV
SV
K
Isotype
TCR
CD40L
BST2
68
91
113
155
Calibration
TCR+ sEV
TCR+ SV
Expression on SV
Size (Scattered light)

Fig.1

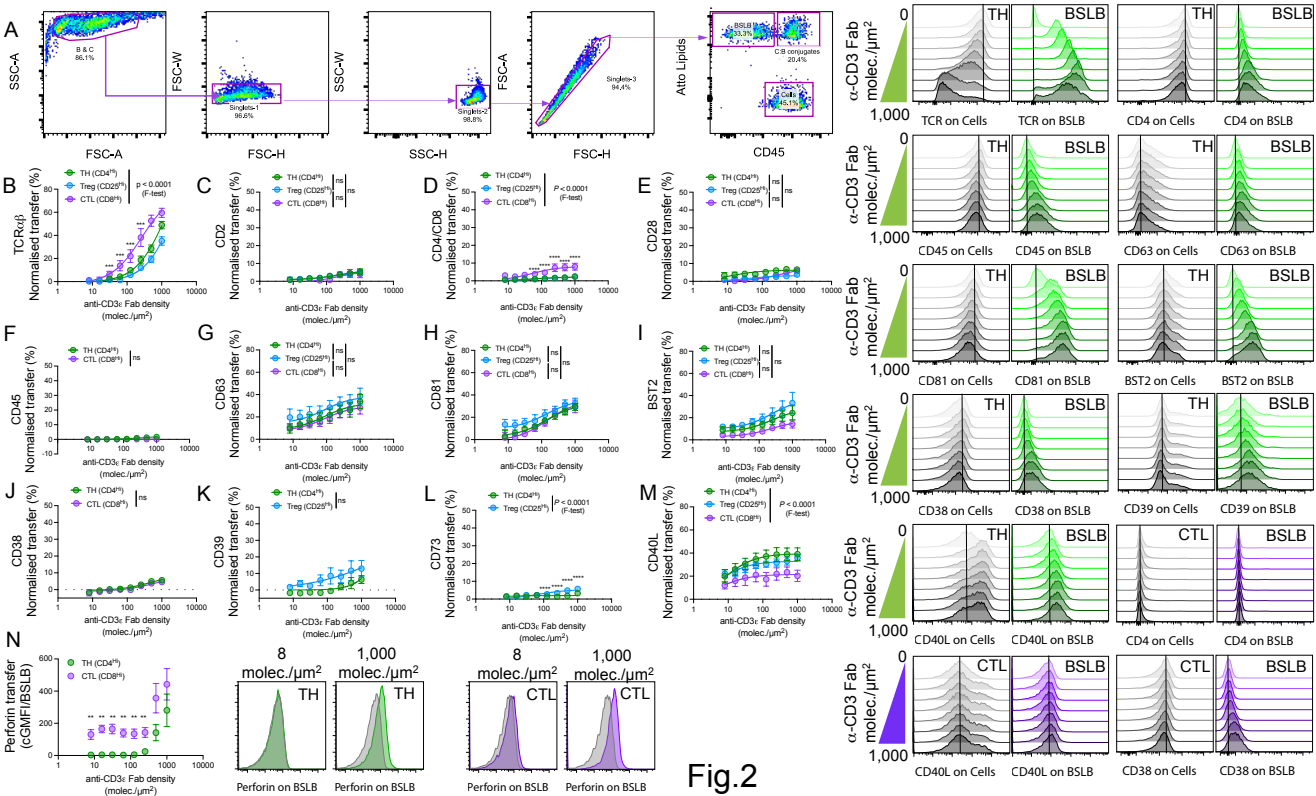
A
SSC-A
FSC-A
B & C
86.1%
FSC-W
FSC-H
Singlets-1
96.6%
SSC-W
SSC-H
Singlets-2
98.8%
FSC-A
FSC-H
Singlets-3
94.4%
Atto Lipids
CD45
BSLB
33.3%
C:B conjugates
20.4%
Cells
45.1%
B
TCRαβ
Normalised transfer (%)
TH (CD4^Hi)
Treg (CD25^Hi)
CTL (CD8^Hi)
p < 0.0001
(F-test)
anti-CD3ε Fab density
(molec./μm²)
C
CD2
ns
D
CD4/CD8
P < 0.0001
(F-test)
E
CD28
F
CD45
CTL (CD8^Hi)
G
CD63
H
CD81
I
BST2
J
CD38
K
CD39
Treg (CD25^Hi)
L
CD73
M
CD40L
N
Perforin transfer
(cGMFI/BSLB)
8
molec./μm²
1,000
molec./μm²
TH
CTL
Perforin on BSLB
α-CD3 Fab
molec./μm²
0
1,000
TH
BSLB
CTL
TCR on Cells
TCR on BSLB
CD4 on Cells
CD4 on BSLB
CD45 on Cells
CD45 on BSLB
CD63 on Cells
CD63 on BSLB
CD81 on Cells
CD81 on BSLB
BST2 on Cells
BST2 on BSLB
CD38 on Cells
CD38 on BSLB
CD39 on Cells
CD39 on BSLB
CD40L on Cells
CD40L on BSLB
CD4 on Cells
CD4 on BSLB
CD38 on Cells
CD38 on BSLB

Fig.2

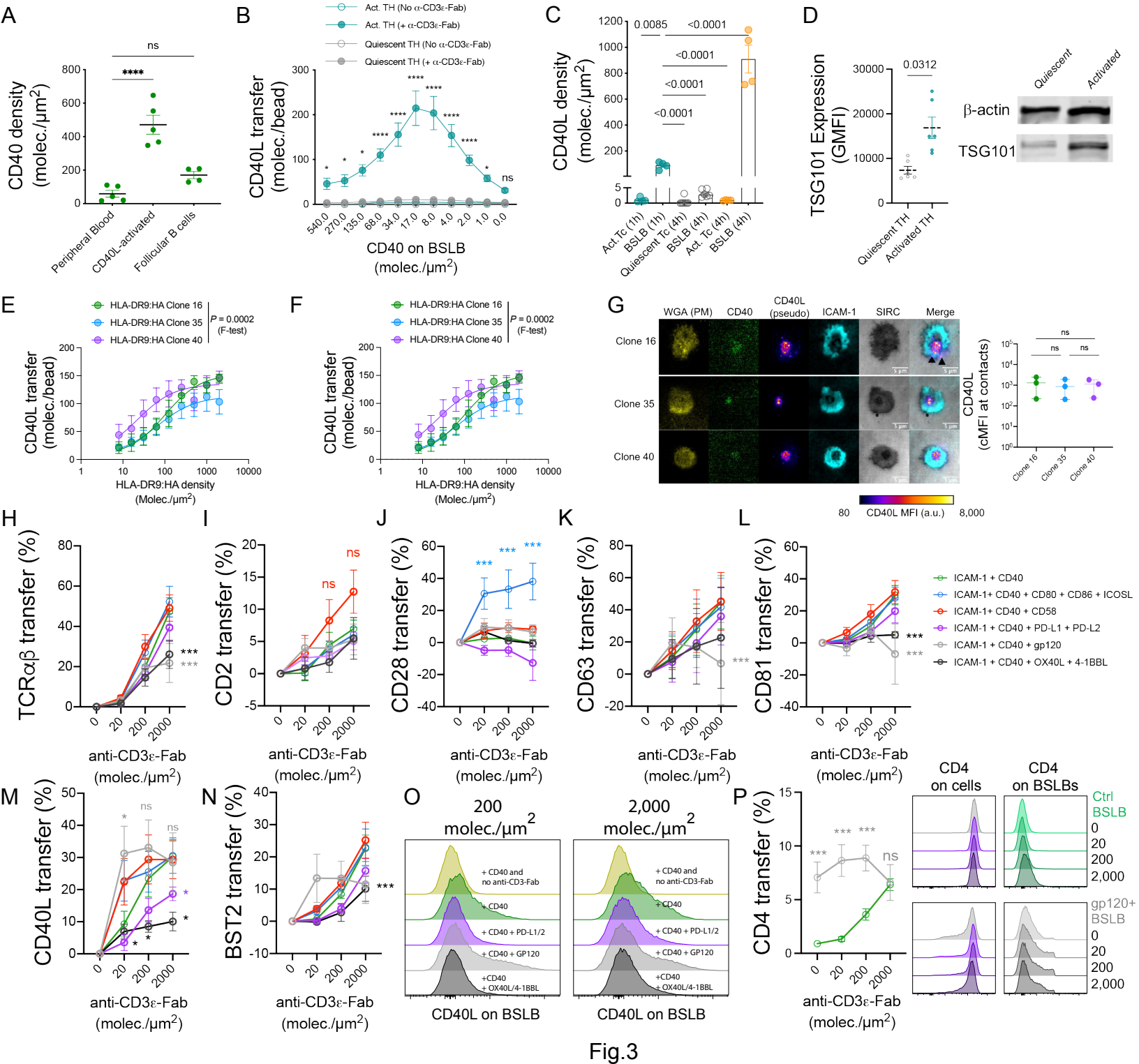
A
CD40 density (molec./μm²)
ns
****
Peripheral Blood
CD40L-activated
Follicular B cells
B
Act. TH (No α-CD3ε-Fab)
Act. TH (+ α-CD3ε-Fab)
Quiescent TH (No α-CD3ε-Fab)
Quiescent TH (+ α-CD3ε-Fab)
CD40L transfer (molec./bead)
CD40 on BSLB (molec./μm²)
C
CD40L density (molec./μm²)
0.0085
<0.0001
Act.Tc (1h)
BSLB (1h)
Quiescent Tc (4h)
BSLB (4h)
Act. Tc (4h)
BSLB (4h)
D
TSG101 Expression (GMFI)
0.0312
Quiescent TH
Activated TH
Quiescent
Activated
β-actin
TSG101
E
HLA-DR9:HA Clone 16
HLA-DR9:HA Clone 35
HLA-DR9:HA Clone 40
P = 0.0002 (F-test)
CD40L transfer (molec./bead)
HLA-DR9:HA density (Molec./μm²)
F
G
WGA (PM)
CD40
CD40L (pseudo)
ICAM-1
SIRC
Merge
Clone 16
Clone 35
Clone 40
CD40L MFI (a.u.)
CD40L (cMFI at contacts)
H
TCRαβ transfer (%)
I
CD2 transfer (%)
J
CD28 transfer (%)
K
CD63 transfer (%)
L
CD81 transfer (%)
anti-CD3ε-Fab (molec./μm²)
ICAM-1 + CD40
ICAM-1+ CD40 + CD80 + CD86 + ICOSL
ICAM-1+ CD40 + CD58
ICAM-1 + CD40 + PD-L1 + PD-L2
ICAM-1 + CD40 + gp120
ICAM-1 + CD40 + OX40L + 4-1BBL
M
CD40L transfer (%)
N
BST2 transfer (%)
O
200 molec./μm²
2,000 molec./μm²
+ CD40 and no anti-CD3-Fab
+ CD40
+ CD40 + PD-L1/2
+ CD40 + GP120
+CD40 + OX40L/4-1BBL
CD40L on BSLB
P
CD4 transfer (%)
CD4 on cells
CD4 on BSLBs
Ctrl BSLB
gp120+ BSLB

Fig.3

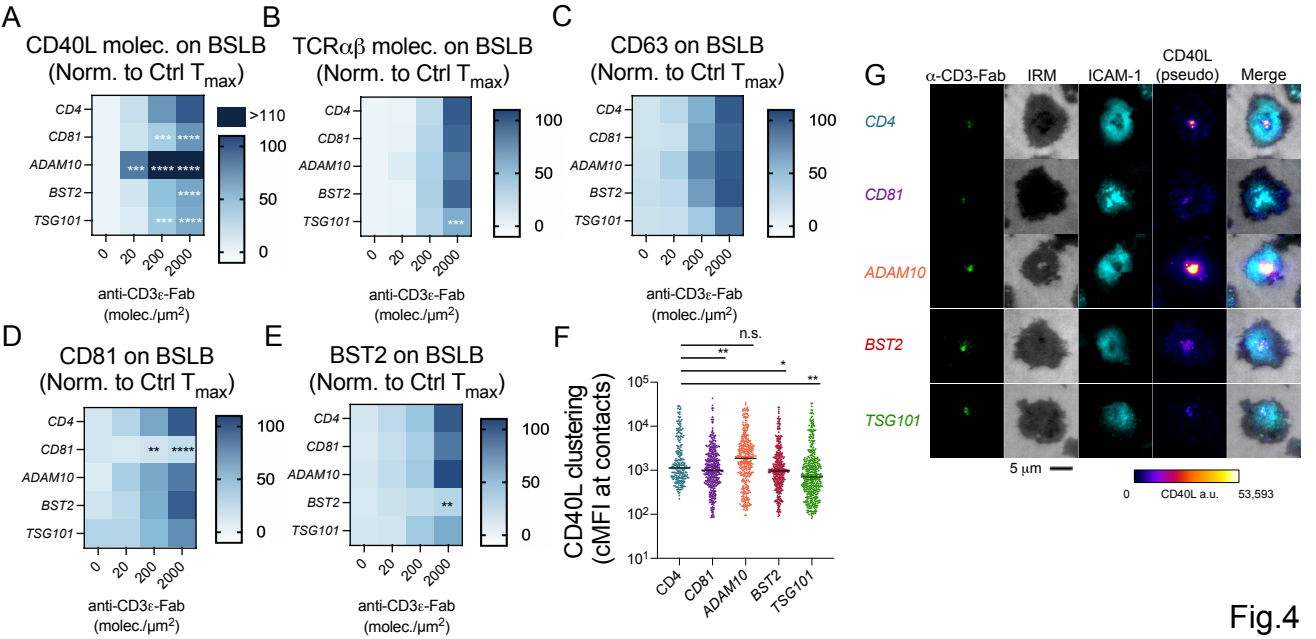
A
CD40L molec. on BSLB
(Norm. to Ctrl T$_{max}$)
B
TCRαβ molec. on BSLB
(Norm. to Ctrl T$_{max}$)
C
CD63 on BSLB
(Norm. to Ctrl T$_{max}$)
CD4
CD81
ADAM10
BST2
TSG101
>110
100
50
0
0
20
200
2000
anti-CD3ε-Fab
(molec./μm^2)
D
CD81 on BSLB
(Norm. to Ctrl T$_{max}$)
E
BST2 on BSLB
(Norm. to Ctrl T$_{max}$)
F
CD40L clustering
(cMFI at contacts)
n.s.
10^5
10^4
10^3
10^2
10^1
G
α-CD3-Fab
IRM
ICAM-1
CD40L
(pseudo)
Merge
5 μm
0
CD40L a.u.
53,593

Fig.4

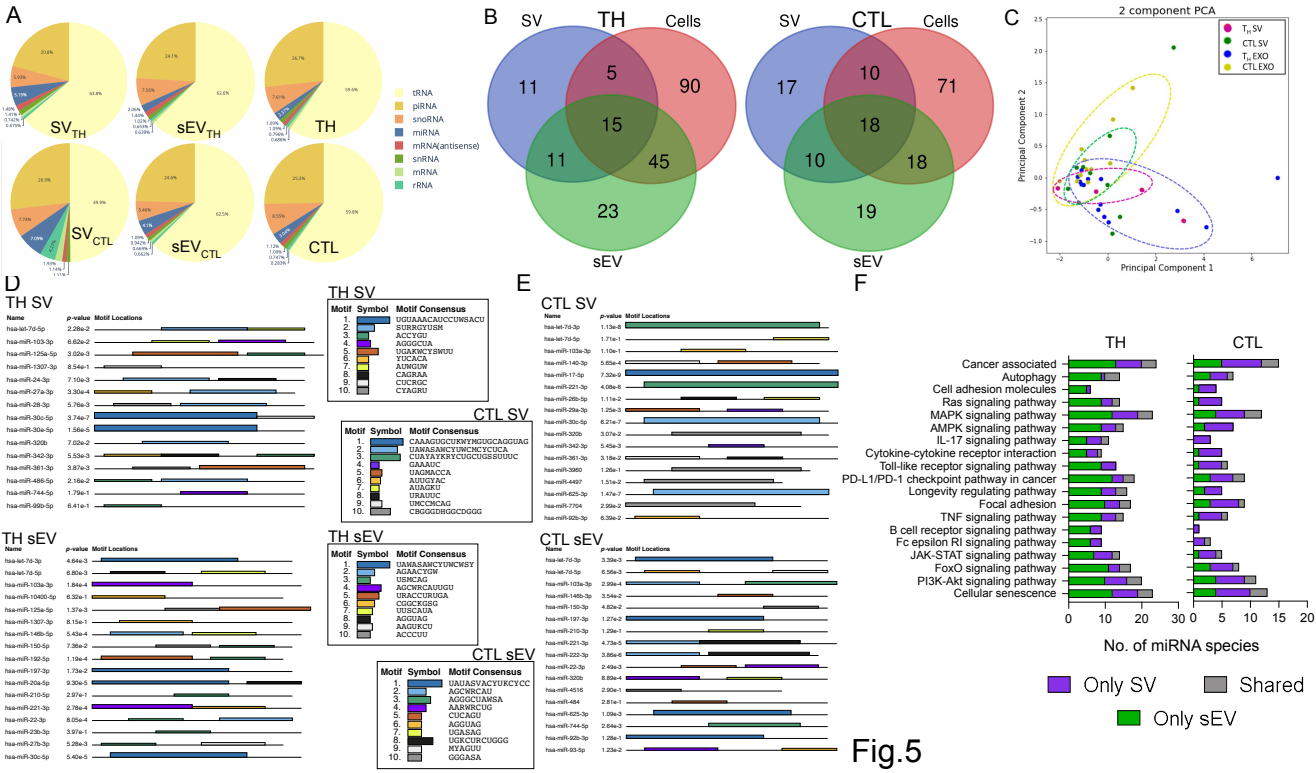
A
SV_TH
sEV_TH
TH
SV_CTL
sEV_CTL
CTL
tRNA
piRNA
snoRNA
miRNA
mRNA(antisense)
snRNA
mRNA
rRNA
B
SV
TH
Cells
11
5
90
15
11
45
23
sEV
SV
CTL
Cells
17
10
71
18
10
18
19
sEV
C
2 component PCA
T_H SV
CTL SV
T_E EXO
CTL EXO
Principal Component 2
Principal Component 1
D
TH SV
Name
p-value
Motif Locations
hsa-let-7d-5p 2.28e-2
hsa-miR-103-3p 6.62e-2
hsa-miR-125a-5p 3.02e-3
hsa-miR-1307-3p 8.54e-1
hsa-miR-24-3p 7.10e-3
hsa-miR-27a-3p 3.30e-4
hsa-miR-28-3p 5.76e-3
hsa-miR-30c-5p 3.74e-7
hsa-miR-30e-5p 1.56e-5
hsa-miR-320b 7.02e-2
hsa-miR-342-3p 5.53e-3
hsa-miR-361-3p 3.87e-3
hsa-miR-486-5p 2.16e-2
hsa-miR-744-5p 1.79e-1
hsa-miR-99b-5p 6.41e-1
TH sEV
hsa-let-7d-3p 4.64e-3
hsa-let-7d-5p 6.80e-3
hsa-miR-103a-3p 1.84e-4
hsa-miR-10400-5p 6.32e-1
hsa-miR-125a-5p 1.37e-3
hsa-miR-1307-3p 8.15e-1
hsa-miR-146b-5p 5.43e-4
hsa-miR-150-5p 7.36e-2
hsa-miR-192-5p 1.19e-4
hsa-miR-197-3p 1.73e-2
hsa-miR-20a-5p 9.30e-5
hsa-miR-210-5p 2.97e-1
hsa-miR-221-3p 2.78e-4
hsa-miR-22-3p 8.05e-4
hsa-miR-23b-3p 3.97e-1
hsa-miR-27b-3p 5.28e-3
hsa-miR-30d-5p 5.40e-5
TH SV
Motif
Symbol
Motif Consensus
1. UGUAAACAUCCUWSACU
2. SURRGYUSM
3. ACCYGU
4. AGGGCUA
5. UGAKWCYSWUU
6. YUCACA
7. AUNGUW
8. CAGRAA
9. CUCRGC
10. CYAGRU
CTL SV
Motif
Symbol
Motif Consensus
1. CAAAGUGCUKWYNGUGCAGGUAG
2. UAWASAWCYUWCMCYCUCA
3. CUAYAYKRYCUGCUGSSUUUC
4. GAAAUC
5. UAGMACCA
6. AUUGYAC
7. AUAGRU
8. URAUUC
9. UNCCMCAG
10. CBGGGDMGGCDGGG
TH sEV
Motif
Symbol
Motif Consensus
1. UAWASAWCYUWCWSY
2. AGAACYGW
3. USMCAG
4. AGCWRCAUUGU
5. URACCURUGA
6. CGGCXGSG
7. UUSCAUA
8. AGGUAG
9. AAGUBCU
10. ACCCUU
CTL sEV
Motif
Symbol
Motif Consensus
1. UAUASVACYUKCYCC
2. AGCWRCAU
3. AGGCCUAMSA
4. AARWRCUG
5. CUCAGU
6. AGGUAG
7. UGASAG
8. UGKCURCUGGG
9. MYAGUU
10. GGGASA
E
CTL SV
Name
p-value
Motif Locations
hsa-let-7d-3p 1.13e-8
hsa-let-7d-5p 1.71e-1
hsa-miR-103a-3p 1.10e-1
hsa-miR-140-3p 5.65e-4
hsa-miR-17-5p 7.32e-9
hsa-miR-221-3p 4.08e-6
hsa-miR-28b-5p 1.11e-2
hsa-miR-29a-3p 1.25e-3
hsa-miR-30c-5p 6.21e-7
hsa-miR-320b 3.07e-2
hsa-miR-342-3p 5.45e-3
hsa-miR-361-3p 3.18e-2
hsa-miR-3960 1.26e-1
hsa-miR-4497 1.51e-2
hsa-miR-625-3p 1.47e-7
hsa-miR-7704 2.99e-2
hsa-miR-92b-3p 6.39e-2
CTL sEV
Name
p-value
Motif Locations
hsa-let-7d-3p 3.39e-3
hsa-let-7d-5p 6.56e-3
hsa-miR-103a-3p 2.99e-4
hsa-miR-146b-3p 3.54e-2
hsa-miR-150-3p 4.82e-2
hsa-miR-197-3p 1.27e-2
hsa-miR-210-3p 1.29e-1
hsa-miR-221-3p 4.73e-5
hsa-miR-222-3p 3.86e-6
hsa-miR-22-3p 2.49e-3
hsa-miR-320b 8.89e-4
hsa-miR-4516 2.90e-1
hsa-miR-484 2.81e-1
hsa-miR-625-3p 1.09e-3
hsa-miR-744-5p 2.64e-3
hsa-miR-92b-3p 1.29e-1
hsa-miR-93-5p 1.23e-2
F
TH
CTL
Cancer associated
Autophagy
Cell adhesion molecules
Ras signaling pathway
MAPK signaling pathway
AMPK signaling pathway
IL-17 signaling pathway
Cytokine-cytokine receptor interaction
Toll-like receptor signaling pathway
PD-L1/PD-1 checkpoint pathway in cancer
Longevity regulating pathway
Focal adhesion
TNF signaling pathway
B cell receptor signaling pathway
Fc epsilon RI signaling pathway
JAK-STAT signaling pathway
FoxO signaling pathway
PI3K-Akt signaling pathway
Cellular senescence
0 10 20 30
0 5 10 15 20
No. of miRNA species
Only SV
Shared
Only sEV

Fig.5